

Relating Modified Newtonian Dynamics to Dark matter - Application to a Virgo-like Galaxy cluster

Odessa Schokker

Bachelor Thesis
Applied Physics &
Applied Mathematics
TU Delft

Delft, January 27th 2022

Monitors: Dr. P.M. Visser
& Dr. S.W.H. Eijt

Contents

| | |
|--|----|
| Tables of constants and variables | iv |
| Abstract | vi |
| 1. Introduction | 1 |
| 2. Gravitational potential in Newtonian Dynamics | 5 |
| 2.1 Gravitational potential for a system of point masses | 5 |
| 2.2 Gravitational potential of a system with an arbitrary mass density | 6 |
| 2.3 Newton's Shell theorem and a spherically symmetric mass density | 7 |
| 2.3.1 Newton's Shell theorem | 7 |
| 2.3.2 Solution for gravitational potential | 7 |
| 3. MOND | 8 |
| 3.1 Deep MOND and full MOND | 9 |
| 4. Mathematical implementation of the model | 10 |
| 4.1 Randomizing galaxy clusters | 10 |
| 4.1.1 Randomize radial coordinates | 10 |
| 4.1.2 Randomize spherical coordinates | 10 |
| 4.2 The Fourier transform | 12 |
| 4.2.1 Fourier transform of the Poisson equation for a point mass | 12 |
| 4.2.2 The fast Fourier transform | 13 |
| 4.3 Examples of potentials in Newtonian Dynamics | 14 |
| 4.3.1 Constant mass distribution | 14 |
| 4.3.2 Isothermal sphere profile | 16 |
| 4.3.3 Navarro-Frenk-White profile | 19 |
| 4.3.4 Gaussian mass distribution | 20 |
| 4.3.5 Multiple spheres with constant mass distribution | 21 |
| 4.4 Helmholtz decomposition with the Fourier transform | 23 |
| 4.5 Solving deep MOND numerically | 24 |
| 4.5.1 Defining zero'th order solution and iterative procedure | 25 |
| 4.6 Solving full MOND numerically | 26 |
| 4.6.1 Defining zero'th order solution and iterative procedure | 27 |
| 5. Study of deep MOND | 29 |
| 5.1 Comparing the deep MOND and the ND potential | 29 |
| 5.2 Acceleration | 36 |
| 5.3 Apparent matter | 38 |
| 5.4 Negative apparent mass | 39 |

| | | |
|-------|--|----|
| 5.4.1 | Changing the radius of galaxies | 39 |
| 5.4.2 | Changing the number of galaxies | 41 |
| 5.4.3 | Discussion of the negative apparent mass | 42 |
| 6. | Study of full MOND | 43 |
| 6.1 | Comparing the full MOND and the ND and deep MOND potential | 43 |
| 6.2 | Acceleration | 48 |
| 6.3 | Apparent matter | 53 |
| 6.4 | Negative apparent matter | 55 |
| 6.4.1 | Changing the radius of galaxies | 55 |
| 6.4.2 | Changing the number of galaxies | 56 |
| 6.4.3 | Discussion of the negative apparent matter in full MOND | 57 |
| 7. | Discussion | 58 |
| 8. | Conclusion and recommendations | 60 |
| | References | 62 |
| | Appendix A: Python code | 63 |
| | Definition of functions | 63 |
| | Code for finding physical quantities | 66 |

Tables of constants and variables

| Constant | Value | Name |
|------------------------|---|------------------------------------|
| a_0 | $1.2 \cdot 10^{-10} \text{m/s}^2$ | Milgrom's constant |
| Mpc | $3.09 \cdot 10^{22} \text{m}$ | Megaparsec |
| $M_{\text{vir-Virgo}}$ | $5.4 \cdot 10^{14} M_{\odot}$ | Virial mass of the Virgo cluster |
| $R_{\text{vir-Virgo}}$ | 1.7Mpc | Virial radius of the Virgo cluster |
| M_{\odot} | $1.99 \cdot 10^{30} \text{kg}$ | Solar mass |
| G | $6.67 \cdot 10^{-11} \text{Nm}^2/\text{kg}^2$ | Gravitational constant |
| k_B | $1.38 \cdot 10^{-23} \text{m}^2\text{kg/s}^2\text{K}$ | Boltzmann constant |
| π | 3.1415 | Pi |

| Variable | Meaning | Formula |
|-----------------------|---|--|
| ρ | Visible mass distribution | |
| ρ_{AM} | Mass distribution of the apparent matter derived by applying the Poisson equation to a MOND potential | |
| ρ_+, ρ_- | + and - component of ρ_{AM} | $\rho_+ + \rho_- = \rho_{\text{AM}}, \rho_+ \geq 0, \rho_- \leq 0, \rho_+\rho_- = 0$ |
| ρ_{ADM} | Mass distribution of the apparent dark matter | $\rho_{\text{AM}} - \rho$ |
| ρ_{DM} | Mass distribution of dark matter computed from lensing observations | |
| M | Total mass of a system | $\iiint_{\mathbb{R}^3} \rho(\mathbf{r}) d\mathbf{f}$ |
| N | Number of galaxies in a galaxy cluster | |
| m | Mass of one galaxy or one pointmass | M/N |
| M_- | Negative apparant mass | $\iiint_{B_{2\text{Mpc}}} \rho_-(\mathbf{r}) d\mathbf{r}$ |
| $M(r)$ | Mass within a ball or radius r with a spherically symmetric mass distribution | |
| R | Radius of a galaxy cluster | |
| R_{sphere} | Radius of a galaxy | |
| ϕ | Actual gravitational potential | |
| ϕ_{ND} | Gravitational potential according to Newtonian Dynamics | |
| ϕ_{M} | Potential derived with some form of MOND | |
| ϕ_{Mdeep} | Potential derived within the deep MOND regime | |
| ϕ_{Mfull} | Potential derived within the full MOND regime | |
| \mathcal{O} | Reference point of a potential | |
| \mathbf{F}_g | Gravitational force | |
| \mathbf{a} | Acceleration | |
| a | Size of \mathbf{a} | |
| \mathbf{g} | Acceleration field in Newtonian Dynamics | $-\nabla \phi_{\text{ND}}$ |
| g | Size of acceleration field in ND | $ \mathbf{g} $ |
| \mathbf{f} | Acceleration field in MOND | $-\nabla \phi_{\text{Mdeep}}$ or $-\nabla \phi_{\text{Mfull}}$ |
| f | Size of acceleration field in MOND | $ \mathbf{f} $ |

| Variable | Meaning | Formula |
|--------------------------------|---|---|
| \mathbf{F} | Vector field in MOND with the direction of \mathbf{f} | $-\nabla \cdot \mathbf{F} = 4\pi G\rho$ |
| F | Size of \mathbf{F} | $ \mathbf{F} $ |
| \mathbf{B} | Divergence free vector field | $\mathbf{F} - \mathbf{g}$ |
| μ | Interpolation function for MOND | |
| n | The number of particles per unit volume | |
| p | The pressure | |
| T | Temperature | |
| σ_V | Velocity dispersion of a galaxy cluster | |
| c | Concentration parameter | |
| A_{NFW} | A constant for the NFW-profile | $\ln(1+c) - \frac{c}{1+c}$ |
| σ | Standard deviation of the Gaussian mass distribution | |
| x, y, z | Cartesian coordinates | |
| r, φ, θ | Spherical coordinates | |
| \mathbf{r} | Location | |
| r | Distance | |
| $\mathcal{F}\{f\}(\mathbf{k})$ | Fourier transform of a function f | |
| $X_{\mathbf{k}}$ | Fast Fourier transform of a sequence $x_{\mathbf{n}}$ | |

Abstract

In this thesis Modified Newtonian Dynamics (MOND) is explored in galaxy clusters similar to the Virgo cluster. MOND is a theory proposed to explain the flat rotation curves of galaxies and the velocities of galaxies within galaxy clusters, as an alternative to the Dark Matter (DM) model. MOND states that Newton's law of gravitation is incorrect at accelerations of the order of and smaller than Milgrom's constant $a_0 = 1.2 \cdot 10^{-10} \text{m/s}^2$ [1].

The MOND potential ϕ_M created by a certain mass distribution ρ satisfies the MOND equation, a non-linear partial differential equation. For accelerations much smaller than a_0 this equation gives a quadratic relation between the gradient of the potential ($\nabla\phi_M$) and the mass distribution ρ , this is called deep MOND. This is much different from the Poisson equation, that infers a linear relation between $\nabla\phi_M$ and the mass sources, and which still holds for accelerations much larger than a_0 [1], referred to as Newtonian Dynamics (ND). For accelerations around a_0 an interpolation of deep MOND and ND is used. It appears that the potential and acceleration in Virgo-like clusters is according to ND at the center, and approaches deep MOND at the edge. Therefore an interpolation function μ is necessary to model such clusters accurately.

When the MOND potential ϕ_M is substituted into the Poisson equation, a new mass distribution is found, the apparent mass distribution ρ_{AM} , which would need to match the actual mass distribution in DM models, which use the Poisson equation. This apparent mass distribution ρ_{AM} is the sum of the actual mass distribution ρ extracted from optical observations and the apparent dark mass distribution ρ_{ADM} , a distribution that is interpreted as a theoretical DM halo. This allows us to compare MOND and DM. With our method, realistic mass configurations of galaxy clusters that are Virgo-like, generate apparent mass distributions ρ_{AM} with regions containing negative mass. The existence, shapes and locations of these regions are in agreement with what Milgrom found [2]. The total mass of the actual mass distribution is $M = 10^{15} M_\odot$, while the sum of the negative mass is $M_- \approx -0.09 \cdot 10^{15} M_\odot = -0.09M$ is approximately 9% of the total mass. Since negative mass is not acceptable, this gives us the opportunity to create conditions to falsify either the MOND model or the DM model.

1. Introduction

In 1933 F. Zwicky determined the speed at which galaxies were moving in galaxy clusters. He found that the galaxies were moving much faster than what could be explained by the visible matter in the cluster according to Newtonian Dynamics (ND). He offered dark matter as a solution, and claimed that the amount of dark matter in the Universe had to be greater than the amount of visible matter. In particular, Zwicky noticed odd behavior of the Coma Cluster. His observations suggested that the dark matter mass in the Coma Cluster needed to be about 400 to 500 times larger than the visible mass to explain the fast motion of the galaxies in the Coma Cluster [3] [4]. According to current much more accurate observations, a dark matter mass that is about 10 times the observed mass would be required.

In the 1970s V. Rubin observed the rotation velocities of stars in the Andromeda Galaxy. She noticed that what happened in the galaxy clusters, also happened in the galaxies themselves. The stars at the outside of the galaxy moved much too fast to be explained by the visible mass in the galaxy. She also proposed that a great amount of dark matter was needed to solve this issue [5].

Around that time people also started to determine rotation curves for disc galaxies from experimental observations. These are curves that plot the orbital speed of stars or gas in that galaxy, against their distance from the galaxy's centre. Assuming ND, we would expect this orbital speed to decrease fastly when the distance to the centre becomes bigger, approximately according to a $r^{-1/2}$ dependence for large r . However, the rotation curves that were created showed that the velocity became constant for larger radii. Figure 3 shows such a rotation curve.

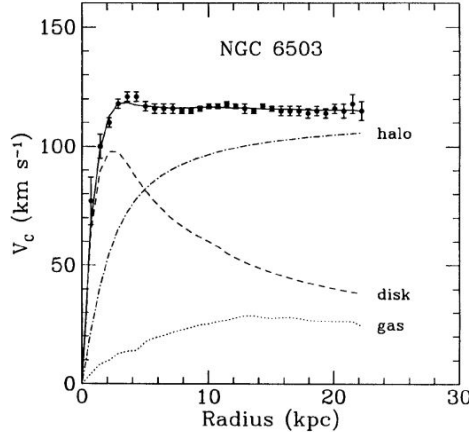


Figure 1: Rotation curve for NGC 6503 [6]. The top line is the observed rotation curve. The other lines show the disk and gas contribution, and halo is the contribution of dark matter to match the data. The total velocity obeys $v_c = \sqrt{v_{\text{disk}}^2 + v_{\text{gas}}^2 + v_{\text{halo}}^2}$.

Figure 1 makes it clear that a large part of observed velocity could be explained by a dark matter halo, and thus the rotation curves supported the idea that ND in combination with the observed mass distributions was not sufficient to explain the behaviour of galaxies and galaxy clusters. Within dark matter models, the mass distributions of these dark matter halos can be reconstructed from weak gravitational lensing observations. In Figure 2 an example of strong gravitational lensing is given for illustrative purposes.

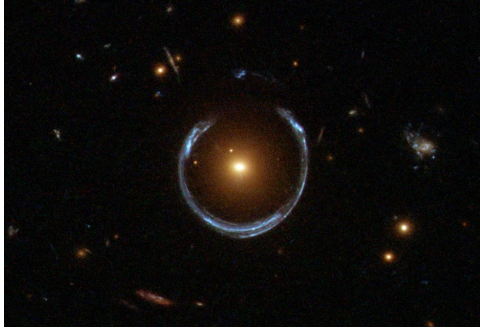


Figure 2: In the Figure we see an example of strong gravitational lensing. A red galaxy has bent the light from a blue galaxy that is located much farther away. The blue galaxy is distorted into a nearly complete ring [7].

A gravitational lens is a large mass, inbetween an observer and a light source. The mass is large enough to bend the light as it travels to the observer. Specifically, weak gravitational lensing is used to find the distribution of the dark matter halos. The difference between weak and strong lensing is based on how much the light is bent by the mass. We will not discuss how the distortion caused by lensing can be measured, and how a distribution of a dark matter halo can be derived from it.

In 1982 M. Milgrom proposed another solution to the problem, Modified Newtonian Dynamics (MOND). The idea was to modify the Newtonian laws, such that dark matter was no longer necessary to explain the observations. At the basis of MOND is the fact that the accelerations in galaxies and galaxy clusters is much lower than the accelerations in solar system, and the assumption that ND is no longer valid at low acceleratoin [1]. Before explaining more about MOND, the next figure is given to illustrate that MOND can explain the observed rotation curves of, in this case, low mass galaxies.

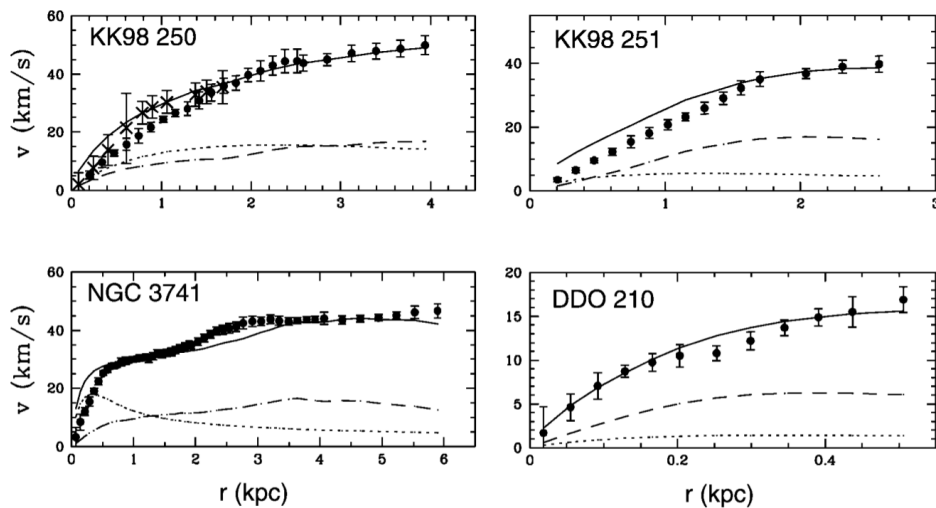


Figure 3: Rotation curve for KK98 250, NGC 3741, KK98 251, DDO 210. The solid curve is the rotation curve according to MOND, the circles show the observed rotation curve. The dotted line represents the ND rotation curve of the disk, and the dashed line of the gas. The crosses in the plot of KK98 250 show the rotation curve obtained with another technique [8].

Both in Figure 1 and Figure 3 the velocities in the rotation curves seem to approach some stable velocity. This is what Milgrom based his theory on. The theory introduces the constant a_0 , an acceleration, with an empirical value of $1.2 \times 10^{-10} \text{ m/s}^2$. It proposes that only when accelerations are much larger than a_0 , ND is a good approximation. Some background information on the gravitational potential in ND will be given in Section 2. When the acceleration is much smaller than a_0 , deep MOND is a good approximation. When the acceleration is about a_0 , some kind of interpolation between ND and MOND is necessary [1]. These scenarios will be explained in Section 3.

One can interpret MOND as a modification of gravity, and as a modification of inertia. When interpreted as modified inertia, there arise some problems, for example conservation of momentum and energy would no longer be valid [9]. This argument has often been used to disregard a new theory, thus therefore we will only consider the interpretation as modified gravity in this thesis. In Section 3 we will discuss what this means.

We will relate MOND and CDM to each other, and with that try to find arguments for or against them. For this we will generate mass distributions of the visible mass in galaxy clusters that are similar to the Virgo cluster. The Virgo cluster is chosen because a lot is known about it from astrophysical observations, and the results can be compared to this knowledge.

To relate MOND and CDM to each other, we will first apply MOND to the modelled mass distribution to find a gravitational potential. We can then find a new mass distribution that would cause this potential according to ND. The difference between this new mass distribution, and the original one, can be treated as a distribution of apparent dark matter. Figure 4 gives an illustration of the steps described.

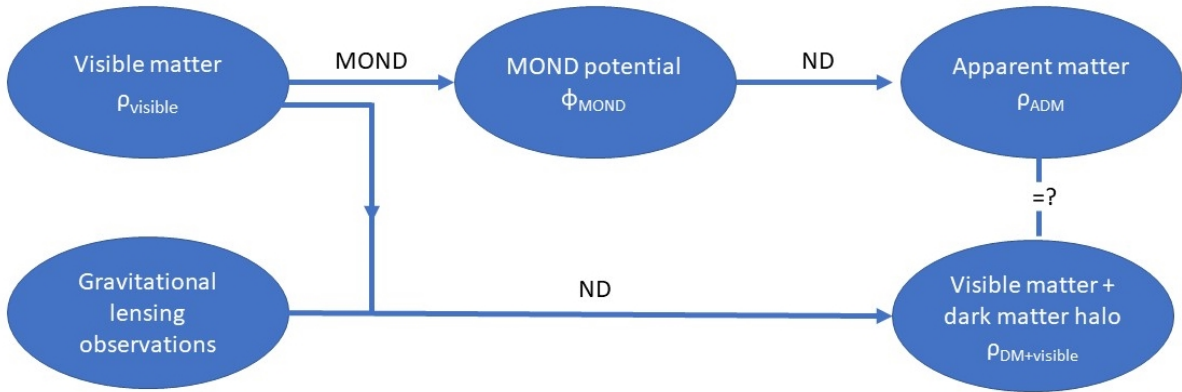


Figure 4: An illustration of the steps taken to find the apparent dark matter mass distribution, and how it relates to the dark matter mass distribution found from gravitational lensing observations.

We are interested in this distribution of apparent mass, since we can compare it to the sum of the visible mass and the dark matter halos that are computed from observations using dark matter models. Since dark matter halos are fitted to observations, if the distribution of apparent mass is similar to this sum, then the MOND potential is similar to the actual potential in galaxy clusters. Thus, we could conclude that MOND is a good model. If the MOND potential gives an apparent mass distribution that is different from the sum of the visible matter and a precisely computed dark matter halo, then MOND is falsified.

When computing the MOND potential, we can either apply deep MOND to the entire region, or an interpolation between ND and MOND that is dependent on the acceleration. In Section 4 we will discuss the mathematical background we will use. Then in Section 5 we will discuss the results of applying deep MOND to a simulated cluster of galaxies with overall properties that are similar to the Virgo cluster, and in Section 6 the application of the interpolation. In Appendix A the code that is used in the thesis is given. The code was based on the code by W. Hajer (to be published on the TU Delft repository).

2. Gravitational potential in Newtonian Dynamics

In this section a derivation of the Newtonian gravitational potential of multiple mass distributions will be given. We will look at a single point mass, a system with an arbitrary mass distribution, and a system with a spherically-symmetric mass distribution.

2.1. Gravitational potential for a system of point masses

In Newtonian dynamics the gravitational force between any two point masses of mass m and M is given by [10]:

$$\mathbf{F}_g = -G \frac{mM}{r^2} \hat{\mathbf{r}}. \quad (1)$$

With G the gravitational constant, and r the distance between the point masses. As we have $\mathbf{F} = m\mathbf{a}$, we can write:

$$\mathbf{a} = -\frac{GM}{r^2} \hat{\mathbf{r}}. \quad (2)$$

It can be shown that the curl of the gravitational acceleration is zero: $\nabla \times \mathbf{a} = 0$. Thus \mathbf{a} can be written as the gradient of a function, $\mathbf{a} = \nabla\phi$. This will now be derived.

By Stokes' theorem we know $\oint \mathbf{a} \cdot d\mathbf{l} = 0$, and thus line integrals of \mathbf{a} from \mathbf{x} to \mathbf{y} are the same for all paths. Therefore we can define a function ϕ as follows:

$$\phi(\mathbf{r}) \equiv -\int_{\mathcal{O}}^{\mathbf{r}} \mathbf{a} \cdot d\mathbf{l}, \quad (3)$$

where \mathcal{O} is a reference point, the point where the potential field is zero, which can be chosen arbitrarily. We call ϕ the gravitational potential. We now write the potential difference between points \mathbf{x} and \mathbf{y} .

$$\phi(\mathbf{y}) - \phi(\mathbf{x}) = -\int_{\mathcal{O}}^{\mathbf{y}} \mathbf{a} \cdot d\mathbf{l} + \int_{\mathcal{O}}^{\mathbf{x}} \mathbf{a} \cdot d\mathbf{l} = -\int_{\mathcal{O}}^{\mathbf{y}} \mathbf{a} \cdot d\mathbf{l} - \int_{\mathbf{x}}^{\mathcal{O}} \mathbf{a} \cdot d\mathbf{l} = -\int_{\mathbf{x}}^{\mathbf{y}} \mathbf{a} \cdot d\mathbf{l}. \quad (4)$$

By the fundamental theorem of line integrals we have the following:

$$\phi(\mathbf{y}) - \phi(\mathbf{x}) = \int_{\mathbf{x}}^{\mathbf{y}} (\nabla\phi) \cdot d\mathbf{l}, \quad (5)$$

which gives us

$$\int_{\mathbf{x}}^{\mathbf{y}} (\nabla\phi) \cdot d\mathbf{l} = -\int_{\mathbf{x}}^{\mathbf{y}} \mathbf{a} \cdot d\mathbf{l}. \quad (6)$$

As this is true for all \mathbf{x} and \mathbf{y} , we need:

$$\mathbf{a} = -\nabla\phi, \quad (7)$$

and thus indeed, \mathbf{a} can be written as the gradient of the scalar ϕ .

We will now find an expression for ϕ for the point mass by substitution of (2) into (3), which gives us:

$$\phi(\mathbf{r}) = GM \int_{\mathcal{O}}^{\mathbf{r}} \frac{\hat{\mathbf{r}}'}{r'^2} \cdot d\mathbf{l}. \quad (8)$$

We choose the reference point \mathcal{O} to be at infinity, resulting in the following expression for the gravitational potential of a point mass M at a distance r :

$$\phi(r) = GM \int_{\infty}^r \frac{dr'}{r'^2} = -\frac{GM}{r'} \Big|_{\infty}^r = -\frac{GM}{r}. \quad (9)$$

The potential of multiple point masses can be calculated by summing the potentials of the singular point masses. For point masses m_1, m_2, \dots, m_n , at locations $\mathbf{x}_1, \mathbf{x}_2, \dots, \mathbf{x}_n$, we get the following potential at location \mathbf{r} ;

$$\phi(\mathbf{r}) = -\frac{Gm_1}{\|\mathbf{r} - \mathbf{x}_1\|} - \frac{Gm_2}{\|\mathbf{r} - \mathbf{x}_2\|} - \dots - \frac{Gm_n}{\|\mathbf{r} - \mathbf{x}_n\|} = -G \sum_{i=1}^n \frac{m_i}{\|\mathbf{r} - \mathbf{x}_i\|}. \quad (10)$$

2.2. Gravitational potential of a system with an arbitrary mass density

We will now derive the potential of a system with a mass density $\rho(\mathbf{x})$ on a region E in \mathbb{R}^3 . For this we will first approximate the potential by dividing region E into $l \times m \times n$ regions. These regions now have a volume $\Delta v = \Delta x \Delta y \Delta z$, and a mass $\rho(\mathbf{x}_{ijk}) \Delta v = \Delta m_{ijk}$, where \mathbf{x}_{ijk} is the center of the box. We now take equation (10), sum over i, j and k , and fill in the previously defined variables. This gives us:

$$\phi(\mathbf{r}) \approx -G \sum_{i=1}^l \sum_{j=1}^m \sum_{k=1}^n \frac{\Delta m_{ijk}}{\|\mathbf{r} - \mathbf{x}_{ijk}\|} = -G \sum_{i=1}^l \sum_{j=1}^m \sum_{k=1}^n \frac{\rho(\mathbf{x}_{ijk}) \Delta v}{\|\mathbf{r} - \mathbf{x}_{ijk}\|} \quad (11)$$

When we take the following limit on the right hand side of equation (11): $l, m, n \rightarrow \infty$, it becomes equal to $\phi(\mathbf{r})$. In this limit the triple sum $\sum_{i=1}^l \sum_{j=1}^m \sum_{k=1}^n$ becomes a triple integral \iiint_E , \mathbf{x}_{ijk} becomes \mathbf{x} and Δv becomes $dv(\mathbf{x}) = dx dy dz$. This results in:

$$\phi(\mathbf{r}) = -G \int_E \frac{\rho(\mathbf{x})}{\|\mathbf{r} - \mathbf{x}\|} dv(\mathbf{x}). \quad (12)$$

This integral equation is equivalent to the differential equation:

$$\nabla \cdot \nabla \phi(\mathbf{x}) = 4\pi G \rho(\mathbf{x}). \quad (13)$$

This equation is called the Poisson equation.

2.3. Newton's Shell theorem and a spherically symmetric mass density

We now consider a system that has a spherically symmetric mass density $\rho(r)$. For this we first consider Newton's Shell theorem.

2.3.1. Newton's Shell theorem

Newton's Shell theorem says that when considering gravity, a spherically symmetric mass distribution affects external objects as if all of its mass is concentrated at the centre of the system. When an object is inside the spherically symmetric system, say at radius r from the centre of the system, the object is only gravitationally affected by the mass inside the ball of radius r around the centre of the system. The mass outside of this ball has no effect on the object.

2.3.2. Solution for gravitational potential

Let us define a function $M(r)$ as the mass of a spherically symmetric system that is found in the ball of radius r around the centre of the system. We get the following:

$$M(r) = \iiint_{B_r} \rho(\tilde{r}) dV = \int_0^{2\pi} \int_0^\pi \int_0^r \rho(\tilde{r}) \tilde{r}^2 \sin(\theta) d\tilde{r} d\theta d\varphi = 4\pi \int_0^r \tilde{r}^2 \rho(\tilde{r}) d\tilde{r}, \quad (14)$$

where B_r is the sphere with radius r around the centre of the system. By Newton's Shell theorem we can now say:

$$\phi(\mathbf{r}) \equiv - \int_{\mathcal{O}}^{\mathbf{r}} \mathbf{a} \cdot d\mathbf{l} = G \int_{\mathcal{O}}^{\mathbf{r}} \frac{M(r')}{r'^2} \hat{\mathbf{r}}' \cdot d\mathbf{l} = G \int_{\mathcal{O}}^r \frac{M(r')}{r'^2} dr'. \quad (15)$$

Substitution of equation (14) into equation (15) gives us:

$$\phi(r) = 4\pi G \int_{\mathcal{O}}^r \frac{\int_0^{r'} \tilde{r}^2 \rho(\tilde{r}) d\tilde{r}}{r'^2} dr'. \quad (16)$$

When the reference point is set at infinity, and $\rho(r) = 0$ when $r > R$, then for $r > R$ we have $M(r) = M$. Here M is the total mass of the system. This gives us the following expression:

$$\phi(r) = G \int_{\infty}^r \frac{M}{r'^2} dr' = - \frac{GM}{r'} \Big|_{\infty}^r = - \frac{GM}{r}. \quad (17)$$

3. MOND

This Section will explain what MOND is. As already stated in the introduction, MOND is based on scales of acceleration. A summary of the theory is that when $a \gg a_0$ the acceleration a of a particle at distance r from a mass M is given by:

$$a = \frac{MG}{r^2}, \quad (18)$$

as according to Newton. When $a \ll a_0$ the acceleration is given by:

$$\frac{a^2}{a_0} = \frac{MG}{r^2}. \quad (19)$$

This regime we call deep MOND. These two equations can be combined to find an expression that describes the transition from ND to deep MOND:

$$\mu\left(\frac{a}{a_0}\right)a = \frac{MG}{r^2}. \quad (20)$$

Here μ is taken such that:

$$\mu(x) = \begin{cases} 1, & \text{if } x \gg 1, \\ x, & \text{if } x \ll 1. \end{cases} \quad (21)$$

As stated in the introduction, MOND can be interpreted as modified gravity and as modified inertia, but we will only consider the modified gravity interpretation. In Newtons theory the acceleration is the gradient of a potential, $\mathbf{a} = -\nabla\phi$, and the potential is a solution of the Poisson equation, which we have already shown in Section 2.2:

$$\nabla \cdot \nabla\phi = 4\pi G\rho. \quad (13 \text{ revisited})$$

In MOND as modified gravity, we still have that $\mathbf{a} = -\nabla\phi$, and the Poisson equation still holds for $a \gg a_0$. However for $a \ll a_0$ Milgrom proposed the following as replacement for the Poisson equation:

$$\nabla \cdot \left(\frac{|\nabla\phi|}{a_0} \nabla\phi \right) = 4\pi G\rho. \quad (22)$$

Combining these two equations gives the MOND equation [1]:

$$\nabla \cdot \left(\mu\left(\frac{|\nabla\phi|}{a_0}\right) \nabla\phi \right) = 4\pi G\rho. \quad (23)$$

Here μ satisfies equation (21).

3.1. Deep MOND and full MOND

In this thesis, we first take $\mu(x) = x$ for simplicity. This is the same as assuming that all accelerations a are much smaller than a_0 , so we assume that the entire region is in the deep MOND regime. By the assumption $\mu(a/a_0) = a/a_0$ the deep MOND potential ϕ_{Mdeep} and the mass distribution ρ satisfy the following equation:

$$\nabla \cdot \left(\frac{|\nabla \phi_{\text{Mdeep}}|}{a_0} \nabla \phi_{\text{Mdeep}} \right) = 4\pi G \rho. \quad (24)$$

We call this the deep MOND equation. In Section 5 we study the behaviour of this simpler model for MOND.

In Section 6 we study what we will call full MOND. The full MOND potential ϕ_{Mfull} and the mass distribution ρ satisfy equation (20), and thus we write the following for the full MOND equation:

$$\nabla \cdot \left(\mu \left(\frac{|\nabla \phi_{\text{Mfull}}|}{a_0} \right) \nabla \phi_{\text{Mfull}} \right) = 4\pi G \rho. \quad (25)$$

Here μ satisfies equation 21.

4. Mathematical implementation of the model

4.1. Randomizing galaxy clusters

When creating randomized galaxies or galaxy clusters we use a spherically symmetric mass distribution function. We need to randomize a radial coordinate, and two spherical coordinates θ and φ ¹. The radial coordinate is dependent on the radial mass distribution function that is chosen for that model. The θ and φ coordinates are always taken from a uniform distribution over a sphere. This Section will address both of these aspects.

4.1.1. Randomize radial coordinates

To randomize radial coordinates the following theorem by Devroye [11] is used:

Theorem 4.1 *‘Let F be a continuous distribution function on R with inverse F^{-1} defined by:*

$$F^{-1}(u) = \inf\{x : F(x) = u, 0 < u < 1\}. \quad (26)$$

If U is a uniform $[0, 1]$ random variable, then $F^{-1}(U)$ has distribution function F .’

With this theorem, random points can be generated according to any mass distribution function $\rho(r)$. Now let $F(r)$ be as follows:

$$F(r) = \frac{1}{M} \iiint_{B_r} \rho(r') dV = \frac{4\pi}{M} \int_0^r r'^2 \rho(r') dr', \quad (27)$$

where B_r is the sphere with radius r , and M is the total mass of the system that can be found using equation (14). Now let u be a random number from the standard uniform distribution on the interval $[0, 1]$, and find r such that $F(r) = u$ or $r = F^{-1}(u)$. Now this r is a random number from the distribution function $f(r) = \frac{\rho(r)}{M}$.

4.1.2. Randomize spherical coordinates

It is important to consider that selecting spherical coordinates θ and φ from a uniform distribution is incorrect. This would give a uniform distribution of points in the ' θ - φ ' plane, but on a sphere this creates a higher concentration of points at the poles, and a lower concentration at the equator. This is the case since $dA = r^2 \sin(\varphi) d\varphi d\theta$ is a function of φ .

This issue can be solved by finding distribution functions $f_\Theta(\theta)$ and $f_\Phi(\varphi)$, that generate a uniform distribution on the unit sphere.

Finding distributions $f_\Theta(\theta)$, $f_\Phi(\varphi)$

Let \mathbf{v} be a point on the unit sphere B_1 , and let f be a uniform distribution on the unit sphere, then $f(\mathbf{v})$ is constant. Now $\iint_{B_1} f(\mathbf{v}) dA = f(\mathbf{v}) \iint_{B_1} dA = 4\pi f(\mathbf{v}) = 1$, so $f(\mathbf{v}) = \frac{1}{4\pi}$.

Now the probability of finding a point in area dA is expressed in two ways. $f(\mathbf{v})dA$ and $f_{\Theta,\Phi}(\theta, \varphi) d\theta d\varphi$. These two probabilities need to be equal to each other, and since $dA = \sin(\varphi) d\varphi d\theta$ and $f(\mathbf{v}) = \frac{1}{4\pi}$ this gives:

¹We use mathematical notation. So θ is the azimuthal angle, and φ is the polar angle.

$$f_{\Theta, \Phi}(\theta, \varphi) = \frac{1}{4\pi} \sin(\varphi). \quad (28)$$

Grimmett and Welsh [12] state the following property: "Whenever the pair X, Y has a joint density function $f_{X,Y}$, the ordinary density function of X and Y may be retrieved immediately since

$$f_X(x) = \int_{-\infty}^{\infty} f_{X,Y}(x, v) dv, \quad (29)$$

and similarly,

$$f_Y(y) = \int_{-\infty}^{\infty} f_{X,Y}(u, y) du." \quad (30)$$

Using this property, gives the following expressions for $f_{\Theta}(\theta)$ and $f_{\Phi}(\varphi)$:

$$f_{\Theta}(\theta) = \int_0^{\pi} f_{\Theta, \Phi}(\theta, \varphi) d\varphi = \frac{1}{2\pi}, \quad (31)$$

$$f_{\Phi}(\varphi) = \int_0^{2\pi} f_{\Theta, \Phi}(\theta, \varphi) d\theta = \frac{\sin(\varphi)}{2}. \quad (32)$$

To randomize the spherical coordinates θ and φ theorem 4.1 is used. First the distribution functions of θ and φ need to be found, which is done by integration:

$$F_{\Theta}(\theta) = \int_0^{\theta} f(\theta') d\theta' = \frac{\theta}{2\pi}, \quad (33)$$

and similarly:

$$F_{\Phi}(\varphi) = \int_0^{\varphi} f(\varphi') d\varphi' = -\frac{\cos(\varphi')}{2} \Big|_0^{\varphi} = \frac{1 - \cos(\varphi)}{2}. \quad (34)$$

Taking U, V as standard uniform distributions on $[0, 1]$, then by theorem 4.1 $\Theta = F_{\Theta}^{-1}(U)$, and $\Phi = F_{\Phi}^{-1}(V)$ have the right distributions to give a uniform distribution on the unit sphere. Where for two random numbers u and v , θ and φ are defined as follows:

$$\theta = F_{\Theta}^{-1}(u) = 2\pi u, \quad (35)$$

$$\varphi = F_{\Phi}^{-1}(v) = \arccos(2v - 1). \quad (36)$$

4.2. The Fourier transform

To save computing time, a big part of the integration and differentiation that happens in this thesis is done in the Fourier domain. In this section we will first show how to use the Fourier transform to find the solution to the Poisson equation for a point mass for illustrative purposes. Then we will introduce the fast Fourier transform (FFT), and how we will apply it.

The Fourier transform of a function $h : \mathbb{R}^3 \rightarrow \mathbb{R}$ in three dimensions is defined as follows [13]:

$$\mathcal{F}\{h\}(\mathbf{k}) \equiv (2\pi)^{-3/2} \iiint_{\mathbb{R}^3} h(\mathbf{x}) e^{-i\mathbf{k}\cdot\mathbf{x}} d\mathbf{x}, \quad (37)$$

$$h(\mathbf{x}) \equiv (2\pi)^{-3/2} \iiint_{\mathbb{R}^3} \mathcal{F}\{h\}(\mathbf{k}) e^{i\mathbf{k}\cdot\mathbf{x}} d\mathbf{k}. \quad (38)$$

4.2.1. Fourier transform of the Poisson equation for a point mass

We will derive the Fourier transform of the following equations, to illustrate how the Fourier transform can be used to solve differential equations. We can also use the Fourier transform of the mass distribution and gravitational potential of a point mass, to check whether our Python code for finding solutions to the Poisson equation is working well.

Given are the mass distribution of a point mass, the gravitational potential of a point mass and the Poisson equation.

$$\rho(\mathbf{r}) = M\delta_{(0,0,0)}(\mathbf{r}), \phi(r) = -\frac{GM}{r}, \quad (?? \text{ revisited})$$

$$\nabla \cdot \nabla\phi = 4\pi G\rho. \quad (13 \text{ revisited})$$

Since the Fourier transform is continuous, if a function $h_\epsilon \rightarrow h$, then $\mathcal{F}\{h_\epsilon\} \rightarrow \mathcal{F}\{h\}$ [13]. This fact will be used to derive $\mathcal{F}\{-\frac{GM}{r}\}$ is. We define a function $\phi_\lambda = -\frac{GM}{r}e^{-\lambda r}$, since $\lim_{\lambda \rightarrow 0} -\frac{GM}{r}e^{-\lambda r} = -\frac{GM}{r}$. We will now derive $\mathcal{F}\{h_\lambda\}$.

$$\mathcal{F}\{\phi_\lambda\}(\mathbf{k}) = (2\pi)^{-3/2} \iiint_{\mathbb{R}^3} -\frac{GM}{r} e^{-\lambda r} e^{-i\mathbf{k}\cdot\mathbf{r}} d\mathbf{r} \quad (39)$$

Rewriting the integral in spherical coordinates gives:

$$\mathcal{F}\{\phi_\lambda\}(\mathbf{k}) = -GM(2\pi)^{-3/2} \int_0^{2\pi} \int_0^\pi \int_0^\infty \frac{e^{-\lambda r}}{r} e^{ikr \cos(\theta)} r^2 \sin(\theta) dr d\theta d\varphi. \quad (40)$$

Here $k = |\mathbf{k}|$. Integrating over φ , r and θ gives:

$$\begin{aligned}
\mathcal{F}\{\phi\}(\mathbf{k}) &= -GM(2\pi)^{-1/2} \int_0^\pi \int_0^\infty r e^{r(ik \cos(\theta) - \lambda)} \sin(\theta) dr d\theta \\
&= -GM(2\pi)^{-1/2} \int_0^\pi \int_0^\infty r e^{r(ik \cos(\theta) - \lambda)} \sin(\theta) dr d\theta \\
&= -GM(2\pi)^{-1/2} \int_0^\pi \frac{\sin(\theta)}{(ik \cos(\theta) - \lambda)^2} d\theta \\
\mathcal{F}\{\phi\}(\mathbf{k}) &= -\frac{GM(2\pi)^{-1/2}}{k^2 + \lambda^2}
\end{aligned} \tag{41}$$

Taking the limit $\lambda \rightarrow 0$ gives:

$$\mathcal{F}\{\phi\}(\mathbf{k}) = -GM(2\pi)^{-1/2} k^{-2}. \tag{42}$$

The Fourier transform of the mass distribution of a point mass (?? revisited) is:

$$\mathcal{F}\{\rho\}(\mathbf{k}) = M(2\pi)^{-3/2} \tag{43}$$

Now by the differentiation identity of the Fourier transform we have [13]:

$$\begin{aligned}
\mathcal{F}\{\nabla \cdot \nabla \phi\} &= -k^2 \mathcal{F}\{\phi\} = GM(2\pi)^{-1/2} \\
&= 4\pi G \mathcal{F}\{\rho\} = \mathcal{F}\{4\pi G \rho\}
\end{aligned} \tag{44}$$

And thus, the Poisson equation is satisfied.

4.2.2. The fast Fourier transform

The fast Fourier transform (FFT) is a numerical approximation of the Fourier transform. For values $x_{\mathbf{n}}$ with, the FFT is defined as follows [13]:

$$X_{\mathbf{k}} \equiv \frac{1}{N^3} \sum_{\mathbf{n}=0}^{N-1} x_{\mathbf{n}} e^{-2\pi i \mathbf{k} \cdot \mathbf{n} / N}, \tag{45}$$

$$x_{\mathbf{n}} \equiv \sum_{\mathbf{k}=0}^{N-1} X_{\mathbf{k}} e^{2\pi i \mathbf{k} \cdot \mathbf{n} / N}. \tag{46}$$

Here $\mathbf{N} = (N, N, N)$, and the sum $\sum_{\mathbf{n}=0}^{N-1}$ means summing over all $\mathbf{n} = (n_x, n_y, n_z)$ such that $0 \leq n_x, n_y, n_z \leq N - 1$. The sum $\sum_{\mathbf{k}=0}^{N-1}$ is defined in the same way.

As already stated, the FFT is an approximation of the Fourier transform. When the FFT is generated on a region $E = L \times L \times L \subset \mathbb{R}^3$ with $0 < L < \infty$, it acts as if the values on

\mathbb{R}^3 are periodic with a period of L in all directions. In the neighbourhood of discontinuities, the Gibbs phenomenon can occur [13]. This means that there occur large oscillations near the discontinuity, and thus, the FFT is no good approximation of the Fourier transform at the borders. To ignore the erroneous behaviour in the results of this thesis, if we want to investigate a region $E = L \times L \times L$, then we do all calculations on a region of size $2L \times 2L \times 2L$, with the center of E in the center of this new region.

4.3. Examples of potentials in Newtonian Dynamics

In this section the Newtonian gravitational potential of some systems with a particular mass distribution ρ will be derived. With some of these mass distributions random galaxy clusters will be generated using the techniques discussed in Section 4.1. The radial coordinates of these clusters will be compared with the original mass distributions to check whether the code to generate random clusters works correctly.

The following radially symmetric mass distributions will be discussed. A ball with a constant mass distribution, for illustrative purposes only. The Isothermal sphere profile, a profile based on the ideal gas law and the hydrostatic equilibrium, and the Navarro-Frenk-White profile, a profile used to describe dark matter halos. These distributions are options for generating the random galaxy clusters. Lastly a Gaussian mass distribution will be discussed, since we will use this distribution to model the mass density of the galaxies within the galaxy clusters.

4.3.1. Constant mass distribution

For the derivation of the gravitational potential of a ball with constant mass we use equation (16), set the reference point at infinity, and take $\rho(r)$ as follows:

$$\rho(r) = \begin{cases} \rho_0, & \text{if } r < R, \\ 0, & \text{if } r > R. \end{cases} \quad (47)$$

The exact value of ρ_0 is not so important for the derivation, however it is taken such that the total mass of the system is $M = \frac{4}{3}\pi\rho_0R^3$. First only the region where $r > R$ is considered, here we have:

$$\phi(r) = -\frac{GM}{r}. \quad (17 \text{ revisited})$$

Now the region where $r < R$ is considered. For this the integral is broken into two pieces, inside and outside of the ball. When inside the ball, the mass behaves as follows by equation (14):

$$M(r') = 4\pi \int_0^{r'} \tilde{r}^2 \rho_0 d\tilde{r} = \frac{4}{3}\pi\rho_0 r'^3 = \frac{M}{R^3} r'^3. \quad (48)$$

Filling this into equation (16) and splitting the integral into two gives:

$$\phi(r) = G \int_{\infty}^r \frac{M(r')}{r'^2} dr' = G \int_{\infty}^R \frac{M}{r'^2} dr' + G \int_R^r \frac{Mr'^3}{R^3 r'^2} dr'. \quad (49)$$

Integrating gives:

$$\phi(r) = -\frac{GM}{R} + \frac{GMr'^2}{2R^3} \Big|_R^r, \quad (50)$$

which gives:

$$\phi(r) = -\frac{GM}{R} + \frac{GMr^2}{2R^3} - \frac{GM}{2R} = -\frac{GM}{R} \left(\frac{3}{2} - \frac{1}{2} \frac{r^2}{R^2} \right). \quad (51)$$

Combining equation (51) and (48) gives the gravitational potential:

$$\phi(r) = \begin{cases} -\frac{GM}{R} \left(\frac{3}{2} - \frac{1}{2} \frac{r^2}{R^2} \right), & \text{if } r < R, \\ -\frac{GM}{r}, & \text{if } r > R. \end{cases} \quad (52)$$

Plotting equations (47) and (52) in one graph gives Figure 5. Also a tangent line is added at $r = 2\text{Mpc}$. The slope of the tangent line is the maximum acceleration for this mass distribution according to ND. Here we take $R = 2\text{Mpc}$, and $M = 10^{15}M_{\odot}$, where M_{\odot} is the Solar mass. These values have been based on the Virgo cluster, which has a virial radius $R_{\text{vir}} = 1.7\text{Mpc}$ and a virial mass $M_{\text{vir}} = 5.4 \times 10^{14}M_{\odot}$. [14] (The virial mass is the mass within the virial radius of the system, this is the radius within which the system satisfies the virial theorem. A theorem that relates the average over time of the total kinetic energy to the average over time of the total potential energy, following $2\langle U_{\text{kin}} \rangle = -\langle U_{\text{pot}} \rangle$ for Newtonian gravitational systems.)

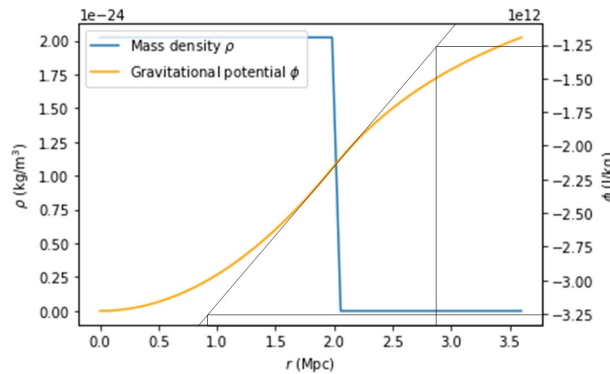


Figure 5: The mass distribution and gravitational potential of a ball with a constant mass distribution, plotted against the distance r from the center. At $r = 2\text{Mpc}$ the tangent line is plotted, which gives a maximum acceleration of approximately $0.3 \times 10^{-10}\text{m/s}^2$. For the plot $R = 2\text{Mpc}$ and $M = 10^{15}M_{\odot}$.

From Figure 5 we find a maximum acceleration of approximately $0.3 \times 10^{-10} \text{m/s}^2$ at $r = 2 \text{Mpc}$, as extracted from the slope of the tangent line. This value is of the order of $a_0 = 1.2 \times 10^{-10} \text{m/s}^2$. What this means exactly is hard to say, since the maximum acceleration was found with ND and for a galaxy cluster of homogeneous mass distribution. However, the mass distribution was based on the Virgo cluster, and thus it is probable that in later calculations for other Virgo-like galaxy clusters (with similar parameters M and R) there are areas in which deep MOND could be applied, while there are also areas in which an interpolation towards ND is necessary.

4.3.2. Isothermal sphere profile

We investigate the isothermal sphere profile since it is a well-known theoretical profile for an idealized model of a galaxy cluster. In the isothermal sphere profile, both the ideal gas law and the hydrostatic equilibrium are satisfied, they are given in equations (54) and (55).

$$\rho = mn, \quad (53)$$

$$p = nk_B T, \quad (54)$$

$$\nabla p = -nm \nabla \phi. \quad (55)$$

Here p is the pressure, n is the number of particles per unit volume, k_B the Boltzmann constant, T the temperature and m the mass of one particle. In our case the particles are the galaxies, and m the mass of a galaxy in the cluster.

If we fill equation (54) into equation (55), we get the following relation:

$$k_B T \nabla n = -nm \nabla \phi. \quad (56)$$

This gives us the following expression for the particle density n :

$$n = ce^{-m\phi/k_B T}. \quad (57)$$

The corresponding mass density is:

$$\rho = mn = mce^{-m\phi/k_B T}. \quad (58)$$

We will try the following mass distribution as a solution to equation (58):

$$\rho(r) = \begin{cases} \frac{\sigma_V^2}{6\pi G} \frac{1}{r^2}, & \text{if } r < R, \\ 0, & \text{if } r > R. \end{cases} \quad (59)$$

Here σ_V is the velocity dispersion of the galaxy cluster. That $\rho(r) = 0$ for $r > R$ is necessary as otherwise $\lim_{r \rightarrow \infty} M(r) = \infty$.

First, we find ϕ by applying equation (16). Considering $r > R$ we have:

$$\phi(r) = -\frac{GM}{r}. \quad (17 \text{ revisited})$$

Here M is the total mass. For $r < R$ we use equation (14) and write:

$$M(r) = 4\pi \int_0^r r'^2 \rho(r') dr' = \frac{4\pi\sigma_V^2}{6\pi G} \int_0^r dr' = \frac{2\sigma_V^2}{3G} r. \quad (60)$$

The total mass of the system is $M = M(R) = \frac{2\sigma_V^2}{3G} R$, and thus:

$$M(r) = \frac{M}{R} r. \quad (61)$$

From the total mass $M = \frac{2\sigma_V^2}{3G} R$ an expression for σ_V can be derived:

$$\sigma_V = \sqrt{\frac{3GM}{2R}}. \quad (62)$$

Substituting equation (61) into equation (16) gives:

$$\begin{aligned} \phi(r) &= -\frac{GM}{R} + \frac{GM}{R} \int_R^r \frac{dr'}{r'} \\ &= -\frac{GM}{R} + \frac{GM}{R} \ln(r') \Big|_R^r \\ &= -\frac{GM}{R} \left(1 - \ln\left(\frac{r}{R}\right)\right). \end{aligned} \quad (63)$$

This results in the following gravitational potential for the Isothermal sphere profile:

$$\phi(r) = \begin{cases} -\frac{GM}{R} \left(1 - \ln\left(\frac{r}{R}\right)\right), & \text{if } r < R, \\ -\frac{GM}{r}, & \text{if } r > R. \end{cases} \quad (64)$$

Now we will check whether equations (59) and (64) satisfy equation (58).

Substituting equations (64) and (59) for $r < R$ into equation (58), and taking the logarithm gives:

$$\ln\left(\frac{\sigma_V^2}{6\pi Gm r^2} \frac{1}{r}\right) = \ln(c) + \frac{m}{k_B T} \frac{GM}{R} \left(1 - \ln\left(\frac{r}{R}\right)\right). \quad (65)$$

Focussing on the r dependent terms gives us:

$$-2 \ln(r) = -\frac{GMm}{k_B T R} \ln r. \quad (66)$$

This gives us the following expression for the temperature T associated with a galaxy cluster of mass M and radius R :

$$T = \frac{GMm}{2k_B R}. \quad (67)$$

Substituting $M = \frac{2\sigma_V^2}{3G}R$ back in gives us what is predicted by the equipartition theorem:

$$3k_B T = m\sigma_V^2. \quad (68)$$

We plot equations (59) and (64) in one graph to get the following figure. Again we take $R = 2\text{Mpc}$, and $M = 10^{15}M_\odot$.

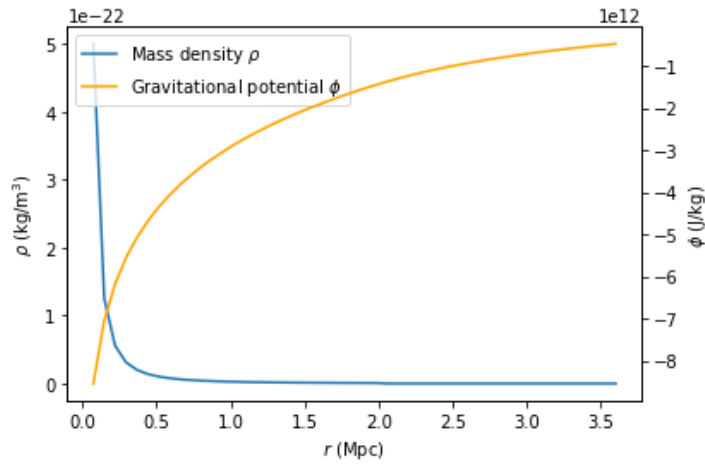


Figure 6: The mass distribution and gravitational potential of the Isothermal sphere profile, plotted against the distance r from the center. The values of M and R are taken the same as in Figure 5.

Next we generate a random galaxy cluster, using the Isothermal sphere profile and the same values for M and R . The cluster consists of $N = 1500$ galaxies, similar to the Virgo cluster [14].

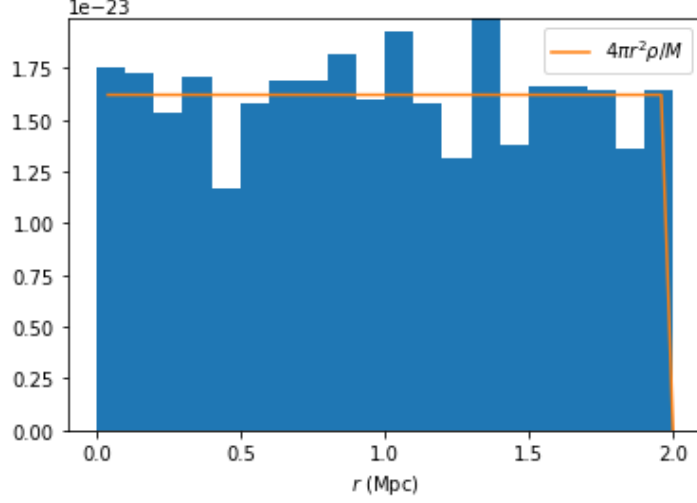


Figure 7: A normalized barplot of the radial coordinates r of the galaxies in a random galaxy cluster that was generated using the Isothermal sphere profile's mass distribution $\rho(r)$. The orange line shows the expected behaviour of the barplot and is given by $4\pi r^2 \rho(r)/M$. The values of M and R are taken the same as in Figure 6.

4.3.3. Navarro-Frenk-White profile

The Navarro-Frenk-White (NFW) profile gives a mass distribution for dark matter halos. It has the following distribution $\rho(r)$:

$$\rho(r) = \begin{cases} \frac{c\rho_{\text{halo}}R_{\text{vir}}^3}{3A_{\text{NFW}}} \frac{1}{r(1+r)^2}, & \text{if } r < R_{\text{vir}}, \\ 0, & \text{if } r > R_{\text{vir}}. \end{cases} \quad (69)$$

Here R_{vir} is the virial radius, $\rho_{\text{halo}} \equiv \frac{3M_{\text{vir}}}{4\pi R_{\text{vir}}^3}$ the mean density of the halo, c the concentration parameter, and $A_{\text{NFW}} = \ln(1+c) - \frac{c}{1+c}$ some constant. For simplicity we take $R_{\text{vir}} = R = 2\text{Mpc}$, $M_{\text{vir}} = M = 10^{15}M_{\odot}$. Furthermore we take $c = 3.8$, based on the Virgo Cluster [15]. Plotting equation (69) and its numerically derived gravitational potential in one graph gives Figure 8:

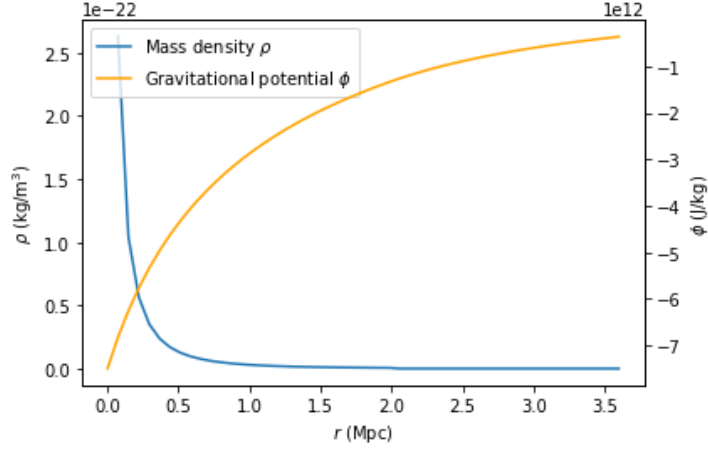


Figure 8: The mass distribution given in equation (69), and the gravitational potential plotted against the distance r from the centre. R and M are taken as in Figure 5 and $c = 3.8$.

We generate a random galaxy cluster using the NFW profile with the same values for M , R , and N , giving the following figure.

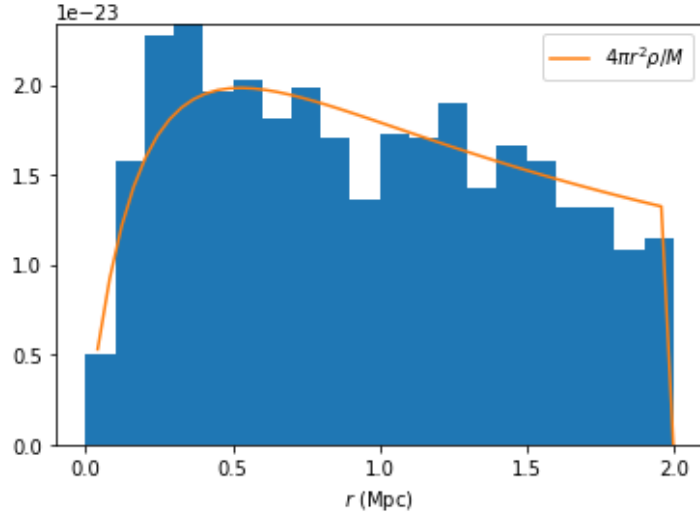


Figure 9: A normalized barplot of the radial coordinates r of the galaxies in a random galaxy cluster that was generated using the NFW profile given in equation (69). The orange line shows the expected behaviour of the barplot and is given by $4\pi r^2 \rho(r)/M$. In this plot R , M and c are taken as in Figure 8.

4.3.4. Gaussian mass distribution

We will use the Gaussian mass distribution to model the mass density inside the galaxies within the galaxy clusters. $\rho(r)$ is defined as follows:

$$\rho(r) = \begin{cases} \frac{M}{(2\pi\sigma^2)^{3/2}} \exp\left(-\frac{r^2}{2\sigma^2}\right), & \text{if } r < R, \\ 0, & \text{if } r > R. \end{cases} \quad (70)$$

Where σ is the standard deviation. This standard deviation is a measure of the radius of a galaxy. Plotting equation (70) and a numerically derived gravitational potential in one graph gives the following figure. We take $R = 2$ Mpc, $M = 10^{15} M_{\odot}$, and $\sigma = 0.4$ Mpc.

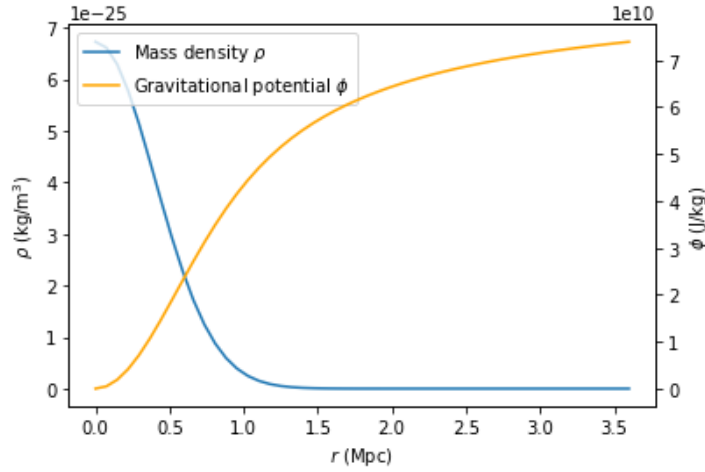


Figure 10: The mass distribution given in equation (70), and the gravitational potential plotted against the distance r from the center. For the plot $R = 2$ Mpc, $M = 10^{15} M_{\odot}$ and $\sigma = 0.4$ Mpc are used.

4.3.5. Multiple spheres with constant mass distribution

In this section the potential of two and 20 galaxies of radius $R = 0.02$ Mpc and total mass $M = 10^{15} M_{\odot}$ is derived. This is done to illustrate that the code for calculating the potential with the Fourier transform works well. Figure 11 gives a one dimensional intersection of the gravitational potential of two galaxies.

In Figure 11 no difference is visible between the exact potential and the potential derived with the fast Fourier transform. Figure 12 shows a two dimensional intersection of the gravitational potential of two galaxies.

In Figure 12 nothing is visible that could cause doubt in the method of deriving the gravitational potential.

In Figure 13 a two dimensional intersection of the gravitational potential of 20 galaxies is given. Their locations were generated with the NFW profile.

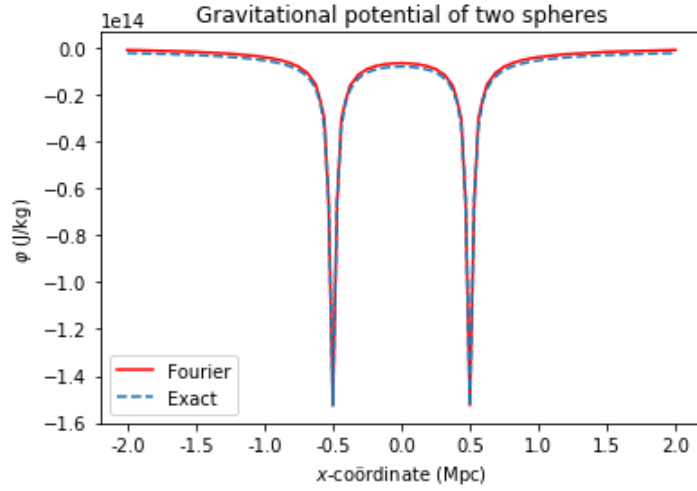


Figure 11: A plot of the gravitational potential of two spherical galaxies along the x -axis with a uniform mass distribution, radius $R = 0.02$ Mpc and total mass $M_{\text{tot}} = 10^{15} M_{\odot}$, placed 1 Mpc apart. The red curve gives the potential derived with the fast Fourier transform with stepsize $dx = 8/256$ Mpc. The dashed blue curve gives the exact potential. The figure shows that calculating the potential with the Fourier transform works well.

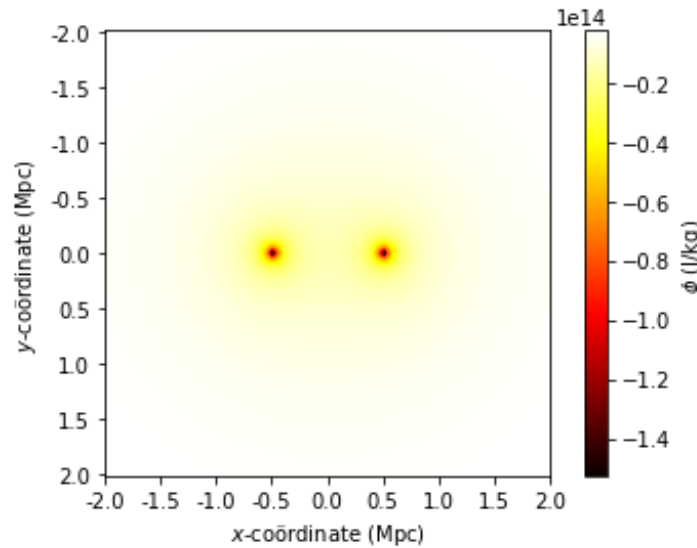


Figure 12: A plot of the gravitational potential of two spherical galaxies with a uniform mass distribution, radius $R = 0.02$ Mpc and total mass $M_{\text{tot}} = 10^{15} M_{\odot}$. The intersection is taken at $z = 0$ Mpc.

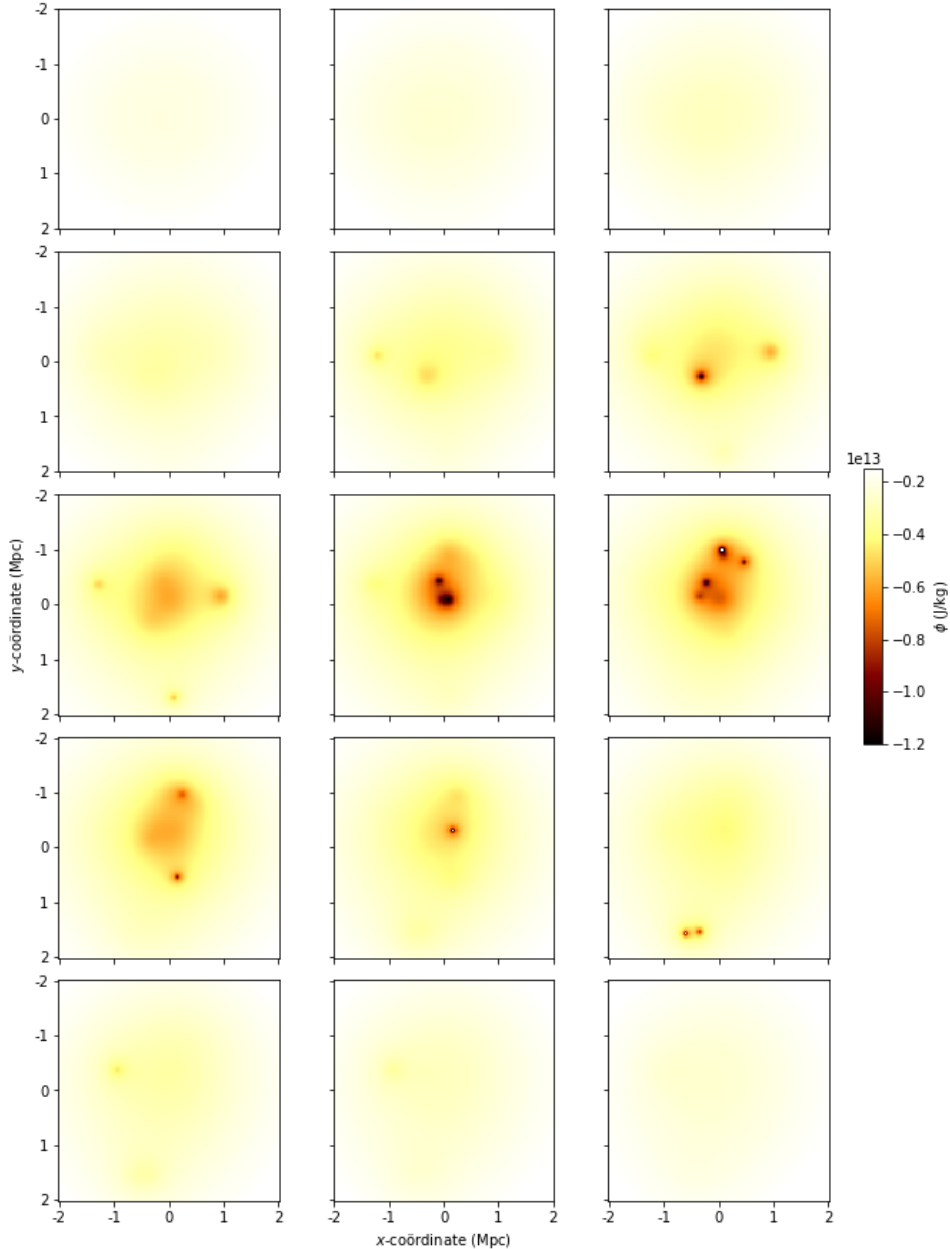


Figure 13: A plot of the gravitational potential of 20 spherical galaxies with a uniform mass distribution, radius $R = 0.02$ Mpc and total mass $M_{\text{tot}} = 10^{15} M_{\odot}$. The intersections are taken at $z = 0 + \frac{n}{4}$ Mpc, with $n = -7, -6, \dots, 6, 7$.

Again, no remarkable observations can be made, and thus we conclude that there are no clear issues with code for deriving the gravitational potential with the fast Fourier transform.

4.4. Helmholtz decomposition with the Fourier transform

In this section it will be explained how to apply the Helmholtz decomposition, a technique that is necessary in the numerical method we will use solving equation (23). Any twice differentiable vector field that decays faster than $1/r$ as $r \rightarrow \infty$ has a Helmholtz decomposition,

where one part is divergence free, and the other part is curl free, and can be written as follows [16]:

$$\mathbf{F} = \mathbf{F}_{//} + \mathbf{F}_{\perp} \quad (71)$$

We introduce the notation that the Fourier transform of any function can be written as follows: $\mathcal{F}\{\mathbf{F}\} = \tilde{\mathbf{F}}$. Taking the Fourier transform of the Helmholtz decomposition of \mathbf{F} gives us:

$$\tilde{\mathbf{F}} = \tilde{\mathbf{F}}_{//} + \tilde{\mathbf{F}}_{\perp} \quad (72)$$

We can also take the Fourier transform of the properties of the curl- and divergence-free parts. This gives us the following relations in the Fourier domain:

$$\nabla \times \mathbf{F}_{//} = \mathbf{0} \iff -i\mathbf{k} \times \tilde{\mathbf{F}}_{//=0} \quad (73)$$

$$\nabla \cdot \mathbf{F}_{\perp} = 0 \iff i\mathbf{k} \cdot \tilde{\mathbf{F}}_{\perp} = 0 \quad (74)$$

To find $\tilde{\mathbf{F}}_{//}$ and $\tilde{\mathbf{F}}_{\perp}$ we use projections. Here we have the following:

$$\tilde{\mathbf{F}}_{//} = \mathbf{k} \frac{\mathbf{k} \cdot \tilde{\mathbf{F}}}{\mathbf{k} \cdot \mathbf{k}} \quad (75)$$

$$\tilde{\mathbf{F}}_{\perp} = \tilde{\mathbf{F}} - \mathbf{k} \frac{\mathbf{k} \cdot \tilde{\mathbf{F}}}{\mathbf{k} \cdot \mathbf{k}} \quad (76)$$

4.5. Solving deep MOND numerically

In this section it will be described how the deep MOND differential equation will be solved numerically. We will find the solution to the system, consisting of the Poisson equation for Newtonian gravity, and the deep MOND equation:

$$\nabla \cdot \nabla \phi_{\text{ND}} = 4\pi G\rho, \quad (13 \text{ revisited})$$

$$\nabla \cdot \left(\frac{|\nabla \phi_{\text{Mdeep}}|}{a_0} \nabla \phi_{\text{Mdeep}} \right) = 4\pi G\rho. \quad (24 \text{ revisited})$$

We will rewrite the system into a system that is easier to work with. For this we define acceleration field \mathbf{f} as follows:

$$\mathbf{f} = -\nabla \phi_{\text{Mdeep}} \quad (77)$$

$$(78)$$

Then equations (13) and (24) are equivalent to the following system:

$$\nabla \cdot \nabla \phi_{\text{ND}} = 4\pi G\rho, \quad (13 \text{ revisited})$$

$$-\nabla \cdot \mathbf{F} = 4\pi G\rho, \quad (79)$$

$$\mathbf{F} = \frac{\mathbf{f}}{a_0}, \quad (80)$$

$$\nabla \times \mathbf{f} = 0. \quad (81)$$

If we now take the Helmholtz decomposition of \mathbf{F} and write $\mathbf{F}_{\parallel} = \mathbf{g}$, and $\mathbf{F}_{\perp} = \mathbf{B}$, then the following holds since $\nabla \cdot \mathbf{B} = 0$:

$$\begin{aligned} -\nabla \cdot \mathbf{F} &= -\nabla \cdot \mathbf{g} - \nabla \cdot \mathbf{B} \\ &= -\nabla \cdot \mathbf{g} = 4\pi G\rho. \end{aligned} \quad (82)$$

And since $\nabla \times \mathbf{g} = 0$, we know:

$$\mathbf{g} = -\nabla \phi_{\text{ND}}. \quad (83)$$

But then we can rewrite the system as follows:

$$-\nabla \cdot \mathbf{g} = 4\pi G\rho, \quad (82 \text{ revisited})$$

$$\mathbf{F} = \mathbf{g} + \mathbf{B}, \quad (84)$$

$$\mathbf{F} = \frac{\mathbf{f}}{a_0}, \quad (80 \text{ revisited})$$

$$\mathbf{g} = -\nabla \phi_{\text{ND}} \quad (83 \text{ revisited})$$

$$\nabla \cdot \mathbf{B} = 0, \quad (85)$$

$$\nabla \times \mathbf{f} = 0. \quad (81 \text{ revisited})$$

This is the system we will be using to apply the iterative method described in the next section.

4.5.1. Defining zero'th order solution and iterative procedure

The system of equations described in the previous paragraph cannot be solved analytically, thus we use an iterative approach that was proposed by Dr. P.M. Visser. We create a sequence \mathbf{f}_n with $n = 0, 1, 2, \dots$ that converges to the solution of system described in the previous Section.

To iterate from the order n solution to order $n + 2$ we need equation (80) and its inverse:

$$\mathbf{F} = \frac{\mathbf{f}}{a_0} \quad (80 \text{ revisited})$$

$$\mathbf{f} = \mathbf{F} \sqrt{\frac{a_0}{F}} \quad (86)$$

For the zero'th order solution we take $\mathbf{B}_0 = \mathbf{0}$, which gives us $\mathbf{F}_0 = \frac{f_0}{a_0} \mathbf{f}_0 = \mathbf{g}$. Applying equation (86) gives us:

$$\mathbf{f}_0 = \mathbf{g} \sqrt{\frac{a_0}{g}} \quad (87)$$

Now, for even n , we have that \mathbf{f}_n will in general not be conservative. Thus we take $\mathbf{f}_{n+1} = \mathbf{f}_{n//}$, with $\mathbf{f}_{n//}$ defined according to Helmholtz decomposition.

However for even n , we have that $\mathbf{B}_{n+1} = \mathbf{F}_{n+1} - \mathbf{g}$ is not curl free. Thus we define $\mathbf{B}_{n+2} = \mathbf{B}_{n+1\perp}$ according to Helmholtz decomposition. We then take $\mathbf{F}_{n+2} = \mathbf{g} + \mathbf{B}_{n+2}$, which gives us an expression for \mathbf{f}_{n+2} .

This \mathbf{f}_{n+2} is closer to the exact solution of the deep MOND equation (24) than \mathbf{f}_n , however it is still not conservative. By iterating the steps in this section, \mathbf{f}_n will converge to the exact solution.

4.6. Solving full MOND numerically

As explained in Section 3.1, an interpolation function is necessary to properly satisfy MOND. In this section the same numerical approach will be explained as in the previous Section, now using the following interpolation function satisfying equation (21):

$$\mu(x) = \frac{x}{\sqrt{1+x^2}} \quad (88)$$

Substitution of this μ into equation (25) and adding the Poisson equation gives us the following system:

$$\begin{aligned} \nabla \cdot \nabla \phi_{\text{ND}} &= 4\pi G \rho & (13 \text{ revisited}) \\ \nabla \cdot \left(\frac{|\nabla \phi_{\text{Mfull}}|}{\sqrt{a_0^2 + |\nabla \phi_{\text{Mfull}}|^2}} \nabla \phi_{\text{Mfull}} \right) &= 4\pi G \rho & (89) \end{aligned}$$

We will rewrite the system into a system that is easier to work with. For this we define acceleration field \mathbf{f} as follows:

$$\mathbf{f} = -\nabla \phi_{\text{Mfull}} \quad (90)$$

$$(91)$$

Then equations (13) and (25) are equivalent to the following system:

$$\nabla \cdot \nabla \phi_{\text{ND}} = 4\pi G\rho, \quad (13 \text{ revisited})$$

$$-\nabla \cdot \mathbf{F} = 4\pi G\rho, \quad (79 \text{ revisited})$$

$$\mathbf{F} = \frac{f}{\sqrt{a_0^2 + f^2}} \mathbf{f}, \quad (92)$$

$$\nabla \times \mathbf{f} = 0. \quad (81 \text{ revisited})$$

If we now take the Helmholtz decomposition of \mathbf{F} and write $\mathbf{F}_{\parallel} = \mathbf{g}$, and $\mathbf{F}_{\perp} = \mathbf{B}$, then the following holds since $\nabla \cdot \mathbf{B} = 0$:

$$\begin{aligned} -\nabla \cdot \mathbf{F} &= -\nabla \cdot \mathbf{g} - \nabla \cdot \mathbf{B} \\ &= -\nabla \cdot \mathbf{g} = 4\pi G\rho. \end{aligned} \quad (82 \text{ revisited})$$

And since $\nabla \times \mathbf{g} = 0$, we know:

$$\mathbf{g} = -\nabla \phi_{\text{ND}}. \quad (83 \text{ revisited})$$

But then we can rewrite the system as follows:

$$-\nabla \cdot \mathbf{g} = 4\pi G\rho, \quad (82 \text{ revisited})$$

$$\mathbf{F} = \mathbf{g} + \mathbf{B}, \quad (84 \text{ revisited})$$

$$\mathbf{F} = \frac{f}{\sqrt{a_0^2 + f^2}} \mathbf{f}, \quad (92 \text{ revisited})$$

$$\mathbf{g} = -\nabla \phi_{\text{ND}} \quad (83 \text{ revisited})$$

$$\nabla \cdot \mathbf{B} = 0, \quad (85 \text{ revisited})$$

$$\nabla \times \mathbf{f} = 0. \quad (81 \text{ revisited})$$

This is the system we will be using to apply the iterative method described in the next section.

4.6.1. Defining zero'th order solution and iterative procedure

This system of equations can also not be solved analytically, so we use a similar iterative approach, also proposed by Dr. P.M. Visser. To iterate from the order n solution to order $n + 2$ we need equation (92) and its inverse:

$$\mathbf{F} = \frac{\mathbf{f}}{\sqrt{a_0^2 + f^2}}, \quad (92 \text{ revisited})$$

$$\mathbf{f} = \mathbf{F} \sqrt{\frac{1}{2} + \frac{1}{F} \sqrt{a_0^2 + \frac{F^2}{4}}}. \quad (93)$$

Here $F = |\mathbf{F}|$. For the zero'th order solution we take $\mathbf{B}_0 = \mathbf{0}$, which gives us $\mathbf{F}_0 = \frac{f_0}{\sqrt{a_0^2 + f_0^2}} \mathbf{f}_0 = \mathbf{g}$. Applying equation (93) gives us:

$$\mathbf{f}_0 = \mathbf{g} \sqrt{\frac{1}{2} + \frac{1}{g} \sqrt{a_0^2 + \frac{g^2}{4}}}. \quad (94)$$

Now again for n even, \mathbf{f}_n is not necessarily conservative, and \mathbf{B}_{n+1} is not curl free. By iterating in the same way as in Section 4.5.1, now with equations (92) and (93), \mathbf{f}_n will converge to the exact solution as $n \rightarrow \infty$.

5. Study of deep MOND

In this section we will focus on multiple phenomena in the deep MOND regime. For some initial mass distributions ρ we will first compare the ND potential and the deep MOND potential ϕ_{Mdeep} . Next we will discuss the acceleration f caused by the deep MOND potential. Which is followed by a discussion of the apparent mass distribution ρ_{AM} that is found by applying the poisson equation to the MOND potential.

Although the deep MOND regime is not accurate for the Virgo cluster, it can be useful to analyse it. The behaviour in the deep MOND regime is a good representation for what happens when accelerations are smaller than $a_0 = 1.2 \times 10^{-10} \text{m/s}$, while the Newtonian regime is a good representation for what happens when accelerations are higher.

In the following calculations we defined the visible mass density ρ as follows. We first generate N random coördinates according to the NFW profile, using a virial radius of $R_{\text{vir}} = 2 \text{ Mpc}$, a virial mass of $M_{\text{vir}} = 10^{15} M_{\odot}$ and a concentration parameter of $c = 3.8$. We choose the NFW profile since it is a broadly used mass distribution. The visible mass density of each galaxy is a Gaussian distribution for which we have some standard deviation R_{sphere} . The mass density is cut off at a radius of $5R_{\text{sphere}}$, to save some computing time.

5.1. Comparing the deep MOND and the ND potential

In this section we will compare the gravitational potential ϕ_{ND} and the deep MOND potential ϕ_{Mdeep} for certain mass distributions. We generated some random galaxy clusters according to the previously described method, with $N = 100, 500$ and 1500 galaxies, $R_{\text{sphere}} = 8/256 \text{ Mpc} = 3.125 \cdot 10^{-2} \text{ Mpc}$ ($8/256 \text{ Mpc}$ is the stepsize dx in the used code), and the total mass of the initial mass distribution $M = 10^{15} M_{\odot}$.

$N = 100$

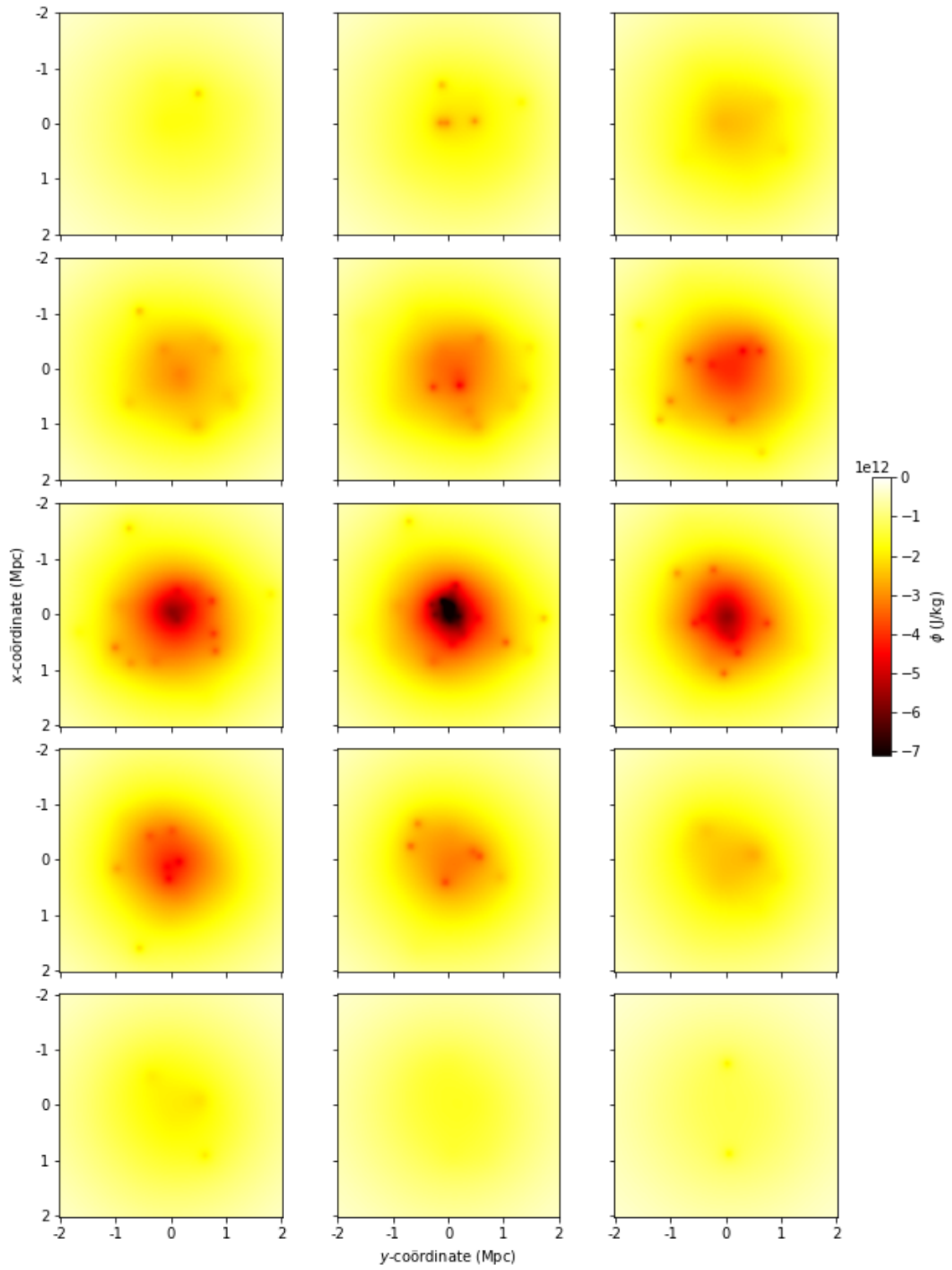


Figure 14: A plot of the ND potential. Here $N = 100$, $R_{\text{sphere}} = 8/256 \text{Mpc}$ and $M = 10^{15} M_{\odot}$. The intersections are taken at $z = 0 + \frac{n}{4} \text{Mpc}$, with $n = -7, -6, \dots, 6, 7$.

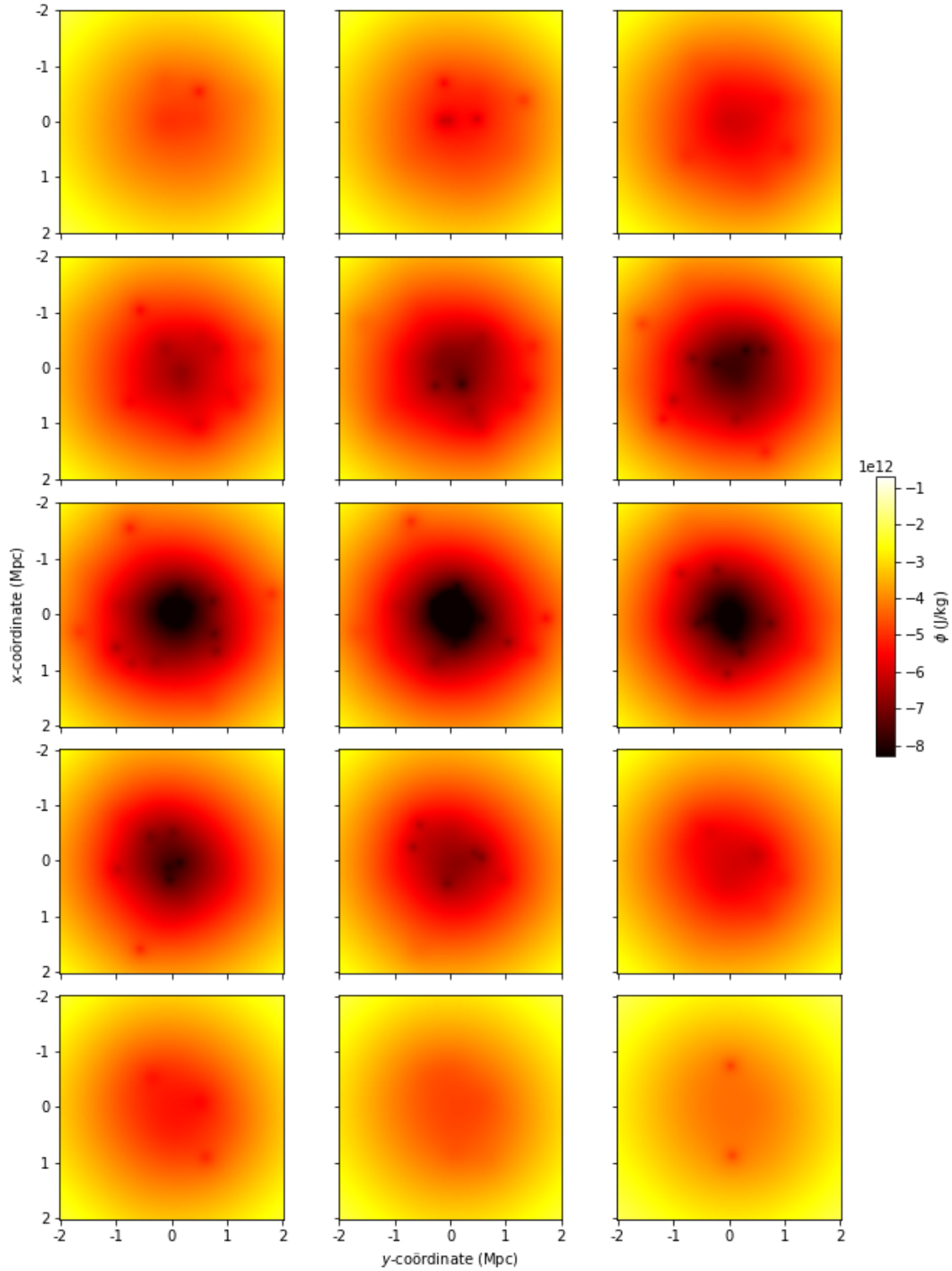


Figure 15: A plot of the deep MOND potential computed with the same initial mass distribution as in Figure 14. The intersections are taken at $z = 0 + \frac{n}{4}$ Mpc, with $n = -7, -6, \dots, 6, 7$. Compared with the ND potential in Figure 14, the deep MOND potential seems less steep at the center, and steeper at the outside of the galaxy cluster.

$N = 500$

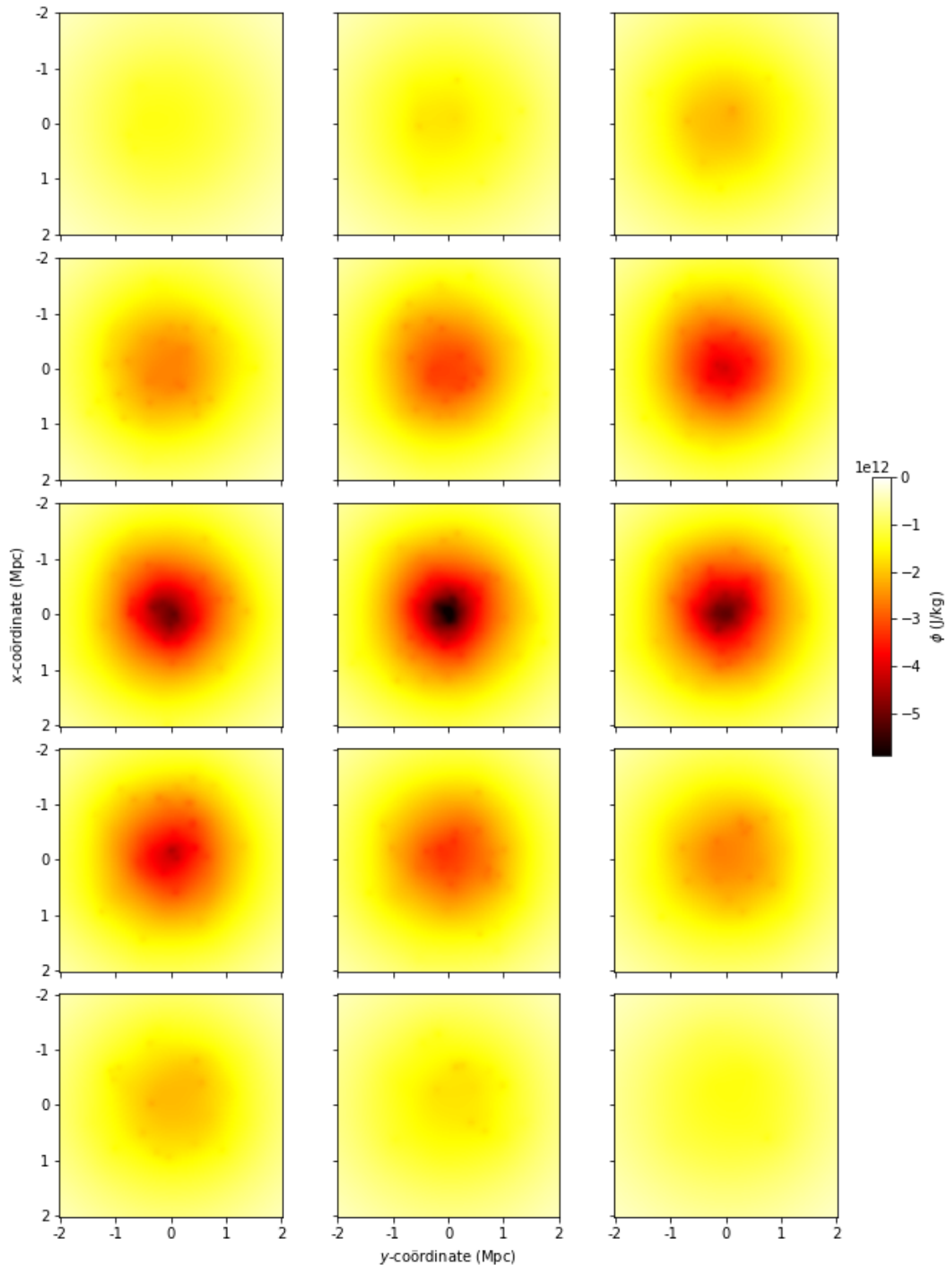


Figure 16: A plot of the ND potential. Here $N = 500$, $R_{\text{sphere}} = 8/256\text{Mpc}$ and $M = 10^{15}M_{\odot}$. The intersections are taken at $z = 0 + \frac{n}{4}\text{Mpc}$, with $n = -7, -6, \dots, 6, 7$.

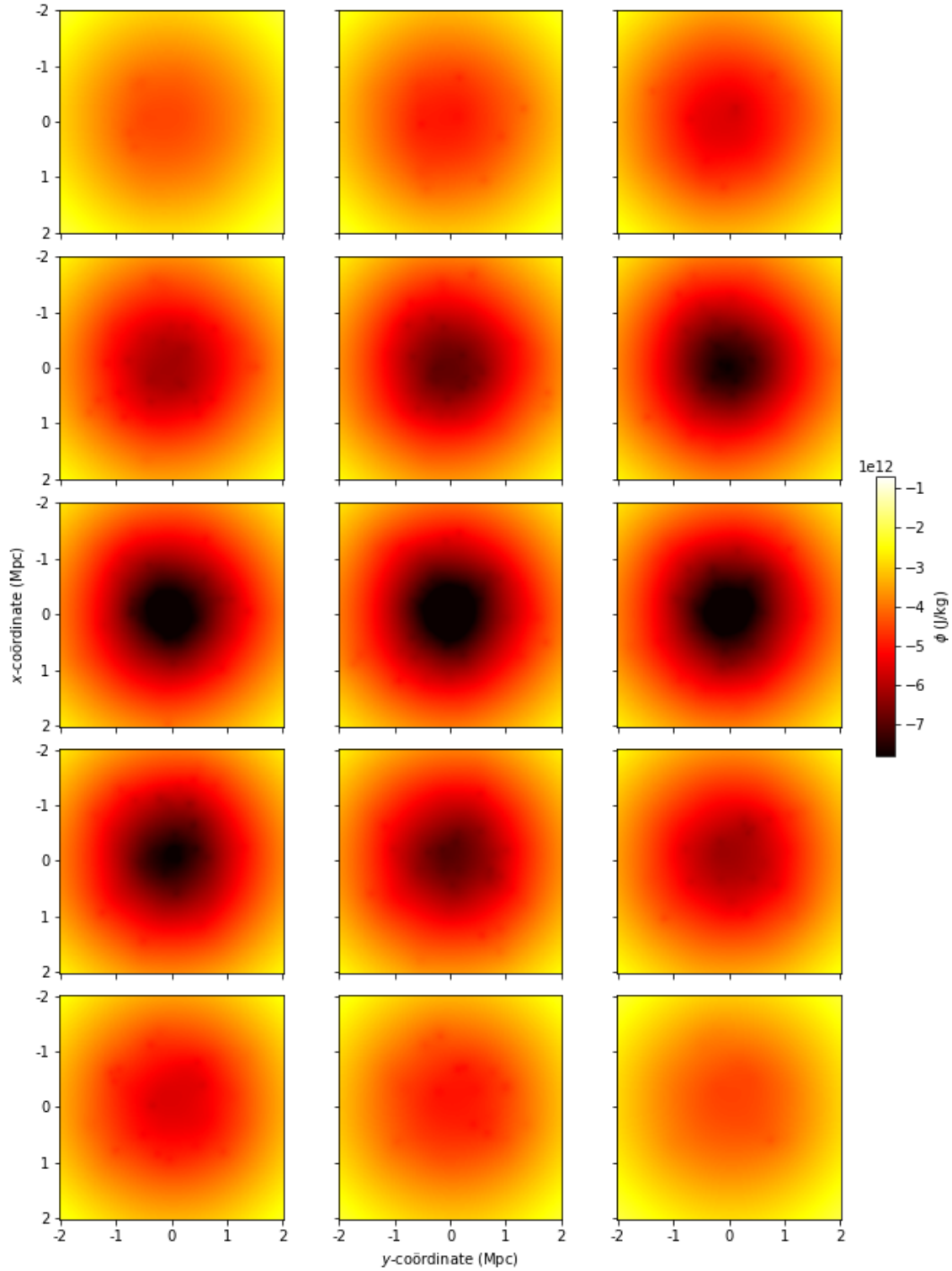


Figure 17: A plot of the deep MOND potential computed with the same initial mass distribution as in Figure 16. The intersections are taken at $z = 0 + \frac{n}{4}$ Mpc, with $n = -7, -6, \dots, 6, 7$. Compared with the ND potential in Figure 16, the deep MOND potential seems less steep at the center, and steeper at the outside of the galaxy cluster.

$N = 1500$

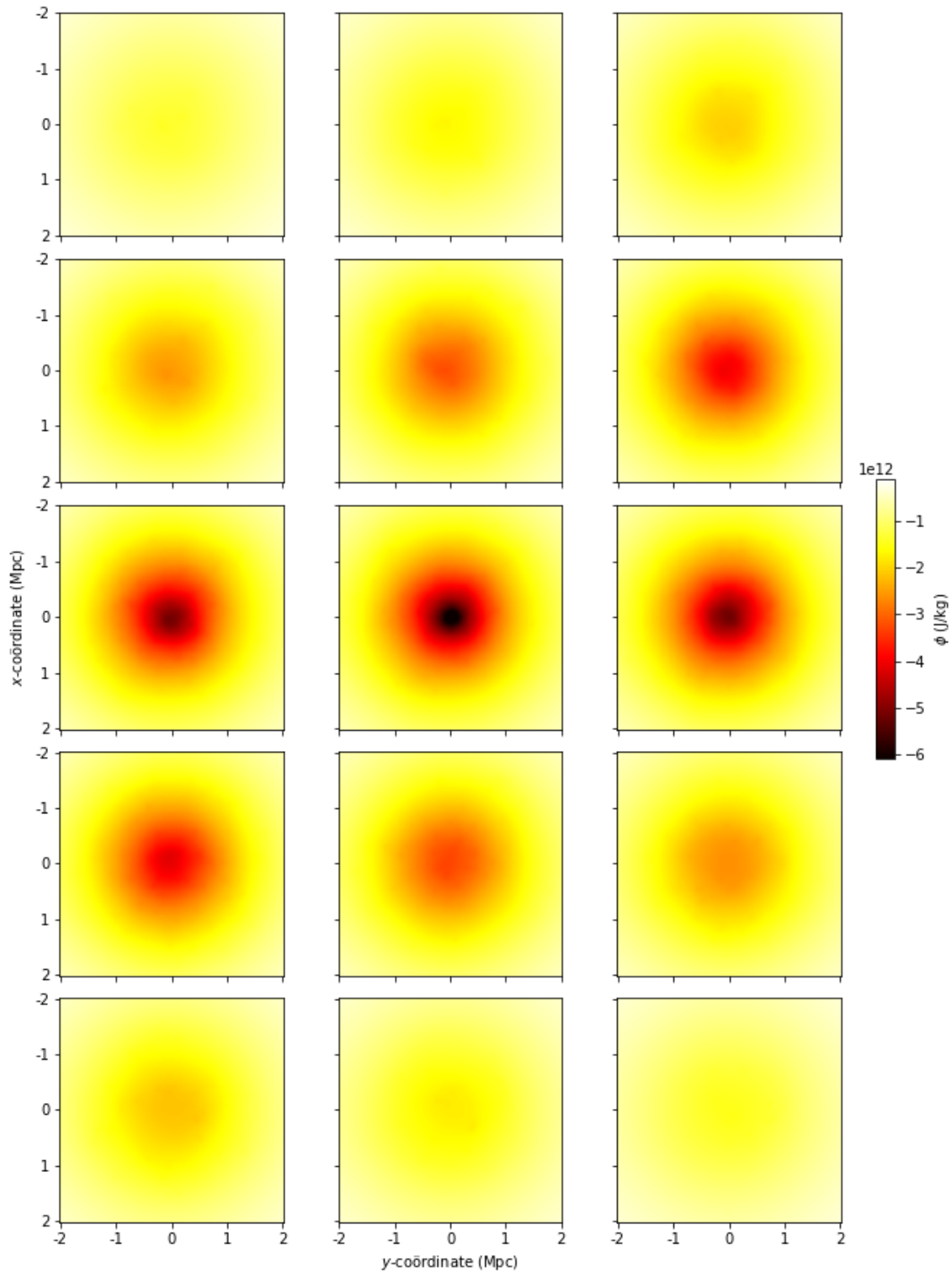


Figure 18: A plot of the ND potential. Here $N = 1500$, $R_{\text{sphere}} = 8/256 \text{Mpc}$ and $M = 10^{15} M_{\odot}$. The intersections are taken at $z = 0 + \frac{n}{4} \text{Mpc}$, with $n = -7, -6, \dots, 6, 7$. The ND potential is almost spherically symmetric.

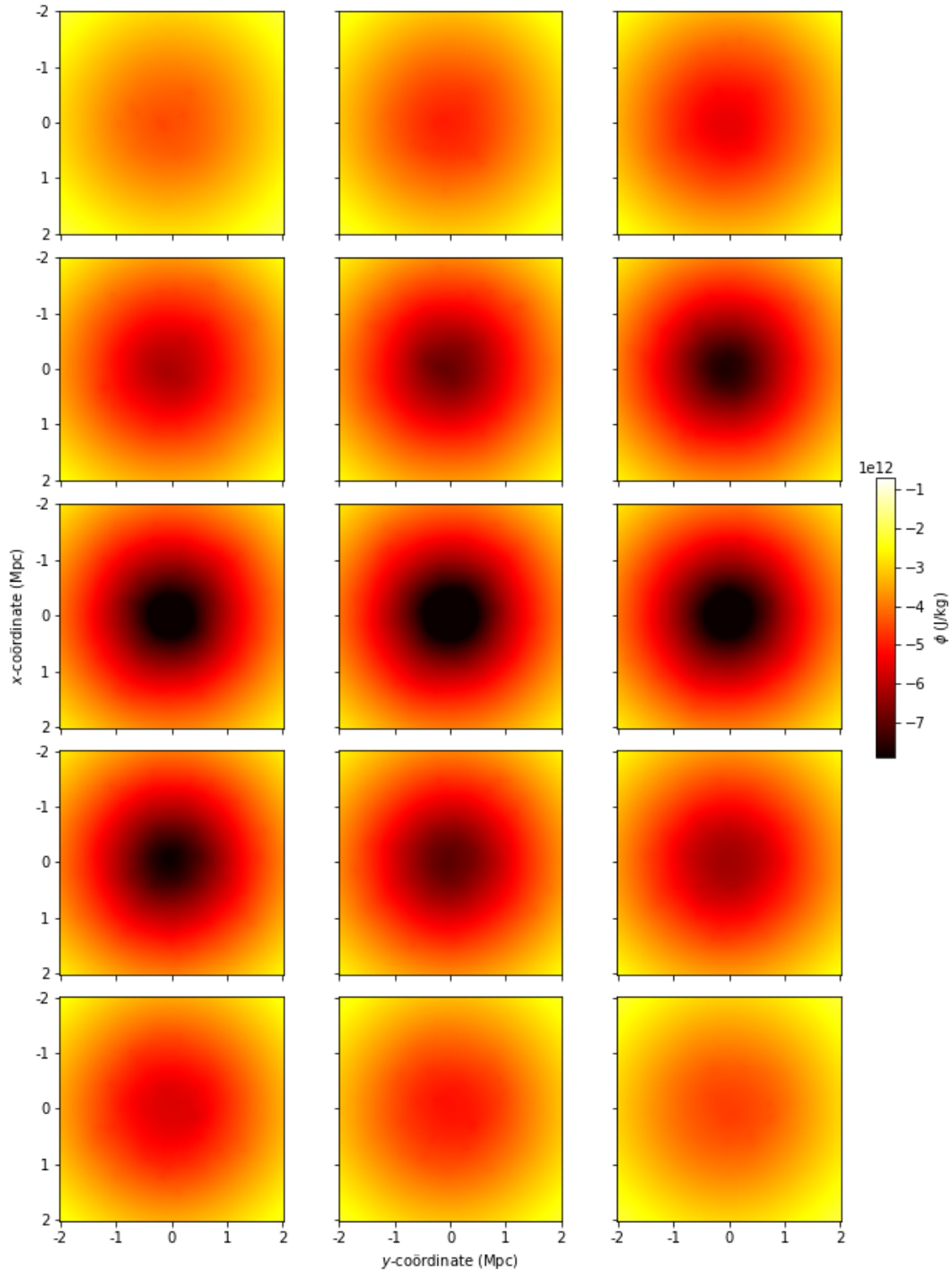


Figure 19: A plot of the deep MOND potential computed with the same initial mass distribution as in Figure 18. The intersections are taken at $z = 0 + \frac{n}{4}$ Mpc, with $n = -7, -6, \dots, 6, 7$. Compared with the ND potential in Figure 18, the deep MOND potential seems less steep at the center, and steeper at the outside of the galaxy cluster. The deep MOND potential is almost spherically symmetric.

The biggest difference between ϕ_{ND} and ϕ_{Mdeep} for $N = 100, 500, 1500$ is the shape of the potential. We will focus on the steepness of the potential. In ND the potential is quite flat at the outside of the galaxy cluster, and very steep in the center. The deep MOND potential is not as steep as the ND potential in the center of the galaxy cluster, but much steeper than the ND potential at the outside of the galaxy cluster. This is what we expect, since MOND predicts that the potential far from a mass is deeper than the potential that ND predicts.

The potentials also have similarities in their shape, in both the deep MOND as the ND potential for $N = 100$ and $N = 500$ the effect of one galaxy on the total potential is clear. Also, for high N both potentials become more spherically symmetric. The gravitational potential and the deep MOND potential are almost spherically symmetric for $N = 1500$.

5.2. Acceleration

In this section we will discuss the accelerations f that are generated by the deep MOND potential ϕ_{Mdeep} for a certain mass distribution. We will argue that the deep MOND approach is not a correct approach to model the behaviour of a galaxy cluster like Virgo. We found the acceleration f by applying the Poisson equation to the deep MOND potential given in Figure 15.

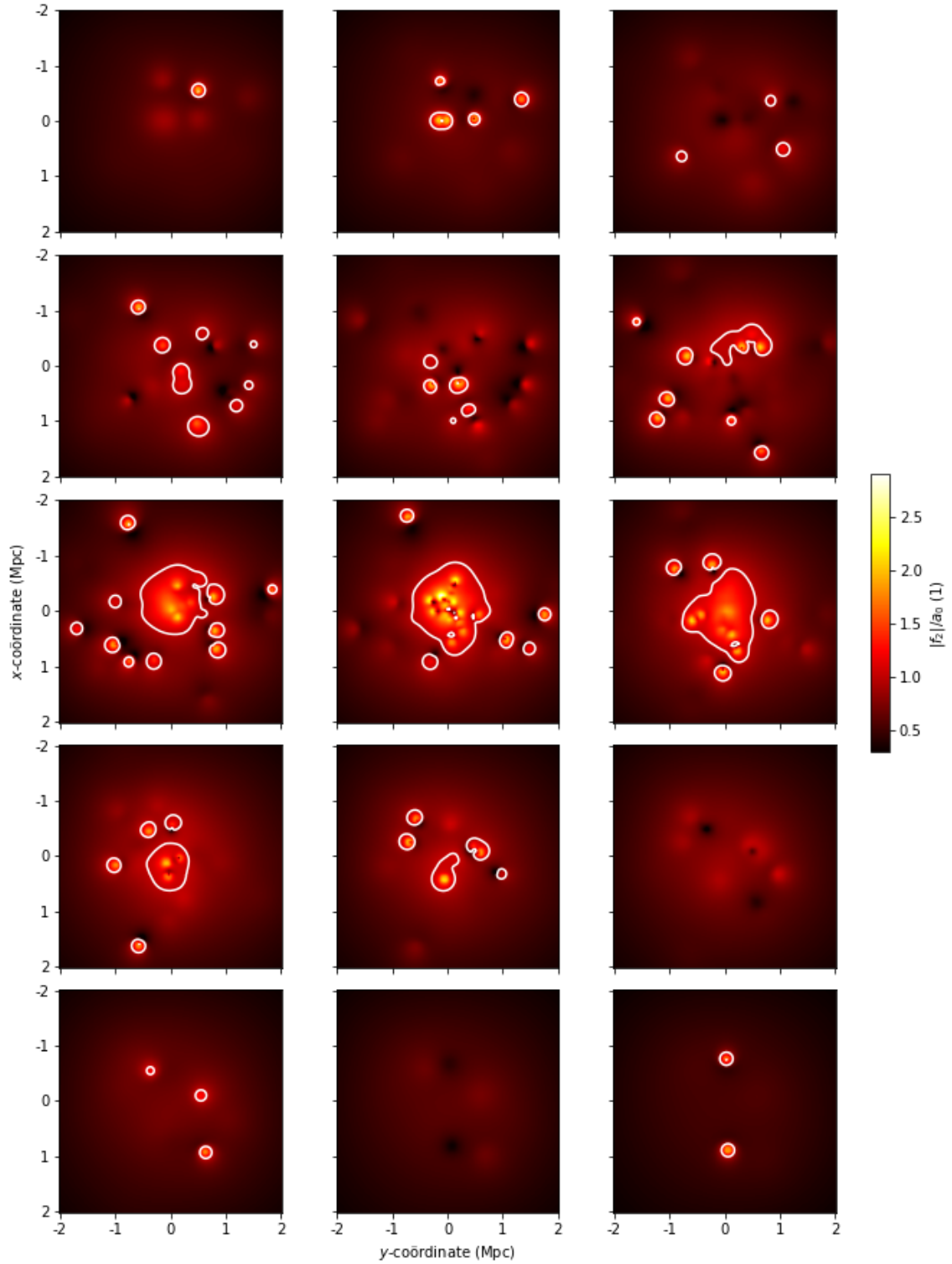


Figure 20: A plot of the size of the acceleration field f divided by a_0 , derived with deep MOND from the same initial mass distribution as in Figure 14. The white curve corresponds to $|f|/a_0 = 1$. The intersections are taken at $z = 0 + \frac{n}{4}$ Mpc, with $n = -7, -6, \dots, 6, 7$. There are large regions where $f > a_0$, but there are also large regions where $f < a_0$.

In Figure 20 it is visible that the acceleration f in a galaxy cluster is both above and below a_0 in large regions. We already predicted this while discussing Figure 5 and the maximum acceleration of the corresponding galaxy cluster according to ND.

For the calculation of the acceleration in Figure 20, we assumed that we could apply the deep MOND regime in the entire galaxy cluster. If this assumption were correct, an acceleration smaller than a_0 would be expected in the entire cluster. Thus we can conclude that the deep MOND regime is no good approximation for the behaviour of a cluster like Virgo.

5.3. Apparent matter

In this section we will discuss the apparent mass distribution ρ_{AM} needed to represent the results of deep MOND in the framework of DM. Figure 21 gives the apparent mass distribution ρ_{AM} belonging to the same mass distribution as used for Figure 14.

In Figure 21 we can see some areas in which $\rho_{AM} \leq 0$, however we cannot clearly see what value the mass density has in those areas. Therefore, we will compute the total negative apparent mass in the next Section. These negative apparent mass density give no reason to doubt the code and mathematics used in this thesis, since Milgrom found negative apparent masses aswell [2].

The regions where $\rho_{AM} \leq 0$ seem to occur inbetween masses, which agrees with what Milgrom found about the shape of regions with negative apparent matter [2]. Furthermore, if we compare Figure 21 to Figure 20, we can see that the areas where $\rho_{AM} \leq 0$ are mostly right outside of the areas where $f \geq a_0$, however, there are also some regions where $\rho_{AM} \leq 0$ and $f \geq a_0$ are the case. Therefore it is hard to determine a clear relation between f and ρ_{AM} . At the outside of the galaxy cluster, where f becomes even smaller, then there is no negative apparent dark mass. This is in agreement with what Milgrom found.

In the figure we also see some dotted crosses that have values around $\rho = 0$. Since these lines are all in the x and y direction, we suspect that they are caused by the fourier transform. A way to lessen this effect is by taking a smaller step size in the fourier transform.

5.4. Negative apparent mass

In this section we will discuss how the smoothness of the initial mass distribution affects the amount of negative apparent mass M_- needed to represent the results of MOND in the framework of DM. It can be shown that for a spherical mass distribution, negative ρ_{AM} cannot happen [2]. To investigate this, we decompose the apparent mass density ρ_{AM} in a $+$ and $-$ component:

$$\rho_{AM} = \rho_+ + \rho_- . \quad (95)$$

Here $\rho_+ \geq 0$ and $\rho_- \leq 0$, furthermore they satisfy $\rho_+ \cdot \rho_- = 0$ everywhere. We compute the negative apparent mass as follows:

$$M_- = \iiint_{B_{2\text{Mpc}}} \rho_- dv . \quad (96)$$

Here $B_{2\text{Mpc}}$ is the sphere with center $(0, 0, 0)$ and radius 2Mpc. We will vary the smoothness of the initial mass distribution ρ in two ways. Firstly by taking some configuration of galaxies, and increasing their radius R_{sphere} , and secondly by generating multiple galaxy clusters with increasing number N of galaxies. Both increasing the radius, as increasing the number of galaxies makes the visible mass distribution ρ smoother and more spherically symmetric. Thus we expect that as R_{sphere} or N is increased, and the initial mass distribution becomes more spherically symmetric, the negative apparent mass M_- becomes smaller.

5.4.1. Changing the radius of galaxies

For the following plot we generated a galaxy cluster with $N = 100$, we generated ρ for different R_{sphere} , and computed ρ_{AM} . The blue circles give the negative apparent mass M_- .

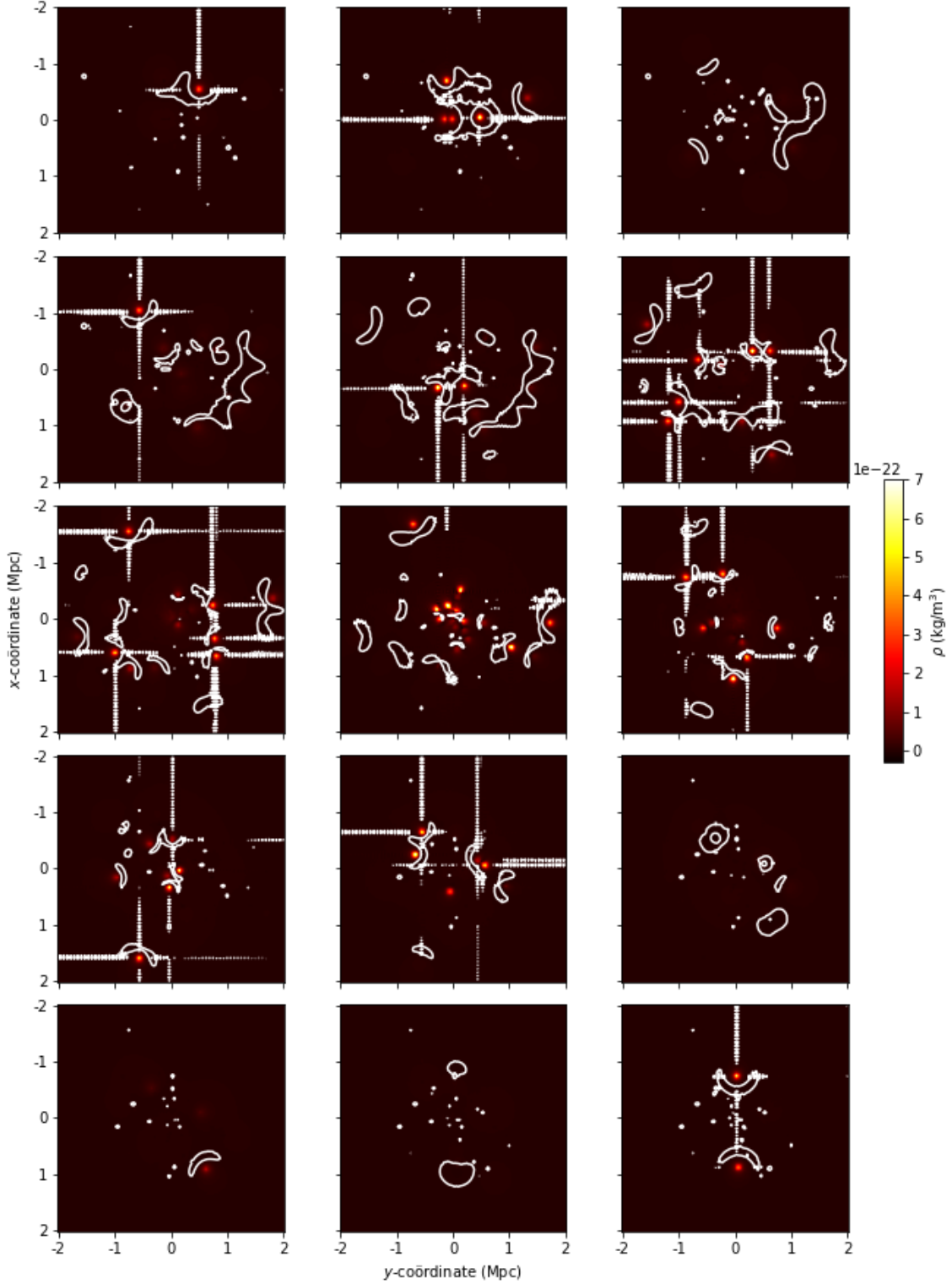


Figure 21: A plot of the apparent mass distribution derived with deep MOND computed with the same initial mass distribution as in Figure 14. The white curve corresponds to $\rho = 0$. The intersections are taken at $z = 0 + \frac{n}{4}$ Mpc, with $n = -7, -6, \dots, 6, 7$. There are significant areas where $\rho_{AM} \leq 0$, and they all seem to be located inbetween galaxies. The dotted crosses are artefacts of the Fourier transform that is used to derive the distribution.

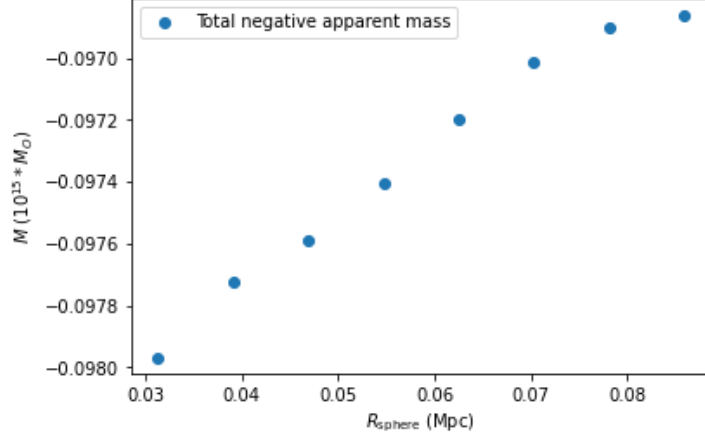


Figure 22: The negative apparent mass M_- , plotted against the radius of the galaxies R_{sphere} in a galaxy cluster with $N = 100$. The blue circles give the sum of the negative part of the apparent mass distribution ρ_- . M_- is derived with deep MOND. There is a clear relation between R_{sphere} and M_- .

We can clearly see that when R_{sphere} is increased, the negative apparent mass M_- becomes smaller.

5.4.2. Changing the number of galaxies

For the following plot we generated multiple galaxy clusters with $R_{\text{sphere}} = 8/256 \text{Mpc}$ for different N , we then computed ρ_- . The blue circles give the negative apparent mass M_- of each galaxy cluster.

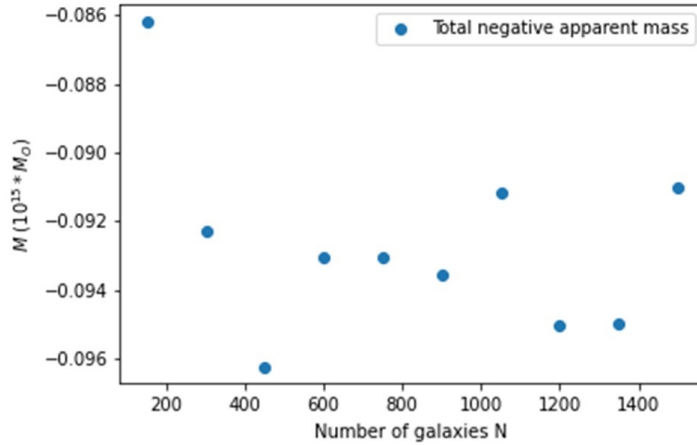


Figure 23: The negative apparent mass M_- , plotted against the number of galaxies N in a galaxy cluster with $R_{\text{sphere}} = 8/256 \text{Mpc}$. The blue circles give the sum of the negative part of the apparent mass distribution ρ_- . M_- is derived with deep MOND. There is no clear relation between N and M_- .

There is no clear relation between the number of galaxies N and the negative apparent mass M_- . This does not contradict with the result of Section 5.4.1 for the following reasons. Firstly,

for each different N a new galaxy cluster is generated, and thus there is a random element to M_- , explaining why Figure 23 looks chaotic. Furthermore, when R_{sphere} is doubled, the volume of the mass distribution ρ that contains mass increases with a factor $2^3 = 8$. However, when N is doubled, this volume increases with a factor 2. Therefore, changing the radius R_{sphere} has a much bigger effect on the smoothness of ρ , than changing N does.

We still expect that increasing N causes M_- to decrease. In followup research M_- could be calculated multiple times for each N , such that an average negative apparent mass M_- can be computed. The contribution of the random element should decrease, and thus if there is a relation between N and M_- , this should become clearer.

5.4.3. Discussion of the negative apparent mass

In this section we have clearly seen that when ρ becomes smoother, the negative apparent mass M_- decreases. However, a galaxy cluster has no smooth visible mass density. In Figure 23 we see that a cluster with $N = 1500$, and galaxies with $R_{\text{sphere}} = 8/256\text{Mpc}$ still has a negative apparent mass of the order $M_- \approx -0.09M$. Since the values for N , R_{sphere} are realistic, we can conclude that, when assuming the deep MOND regime with our method, we can generate realistic mass configurations, that give a significant amount of negative apparent mass.

6. Study of full MOND

In this section we will focus on some results of full MOND. We will use the same mass distributions as in Section 5 for $N = 100, 500, 1500$. We will first discuss the full MOND potential ϕ_{Mfull} of these mass distributions and compare it to ϕ_{ND} and ϕ_{Mdeep} , then the accelerations will be discussed, followed by the apparent mass distributions ρ_{app} . Lastly we will investigate the dependency of the negative apparent mass M_- on the smoothness of the visible mass distribution ρ .

6.1. Comparing the full MOND and the ND and deep MOND potential

In this section we will compare the full MOND potential ϕ_{Mfull} with the ND potential ϕ_{ND} and the deep MOND potential ϕ_{Mdeep} from Section 5.1.

$$N = 100$$

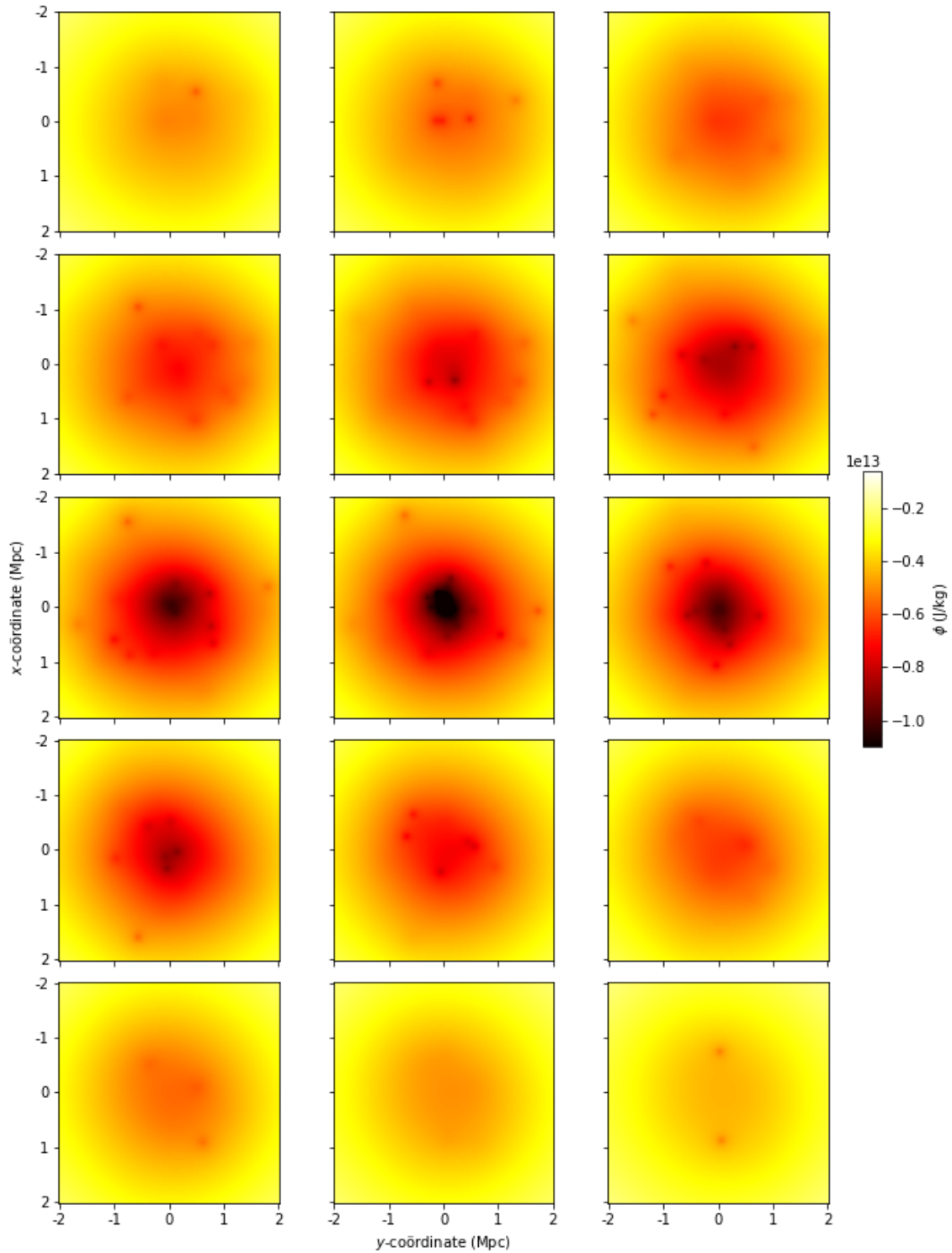


Figure 24: A plot of the full MOND potential, derived from the same initial mass distribution as Figure 14 with $N = 100$. The intersections are taken at $z = 0 + \frac{n}{4}$ Mpc, with $n = -7, -6, \dots, 6, 7$. The full MOND potential seems to follow the shape of the ND potential of Figure 14 at the center of the galaxy cluster, and of the deep MOND potential of Figure 15 at the outside.

$$N = 500$$

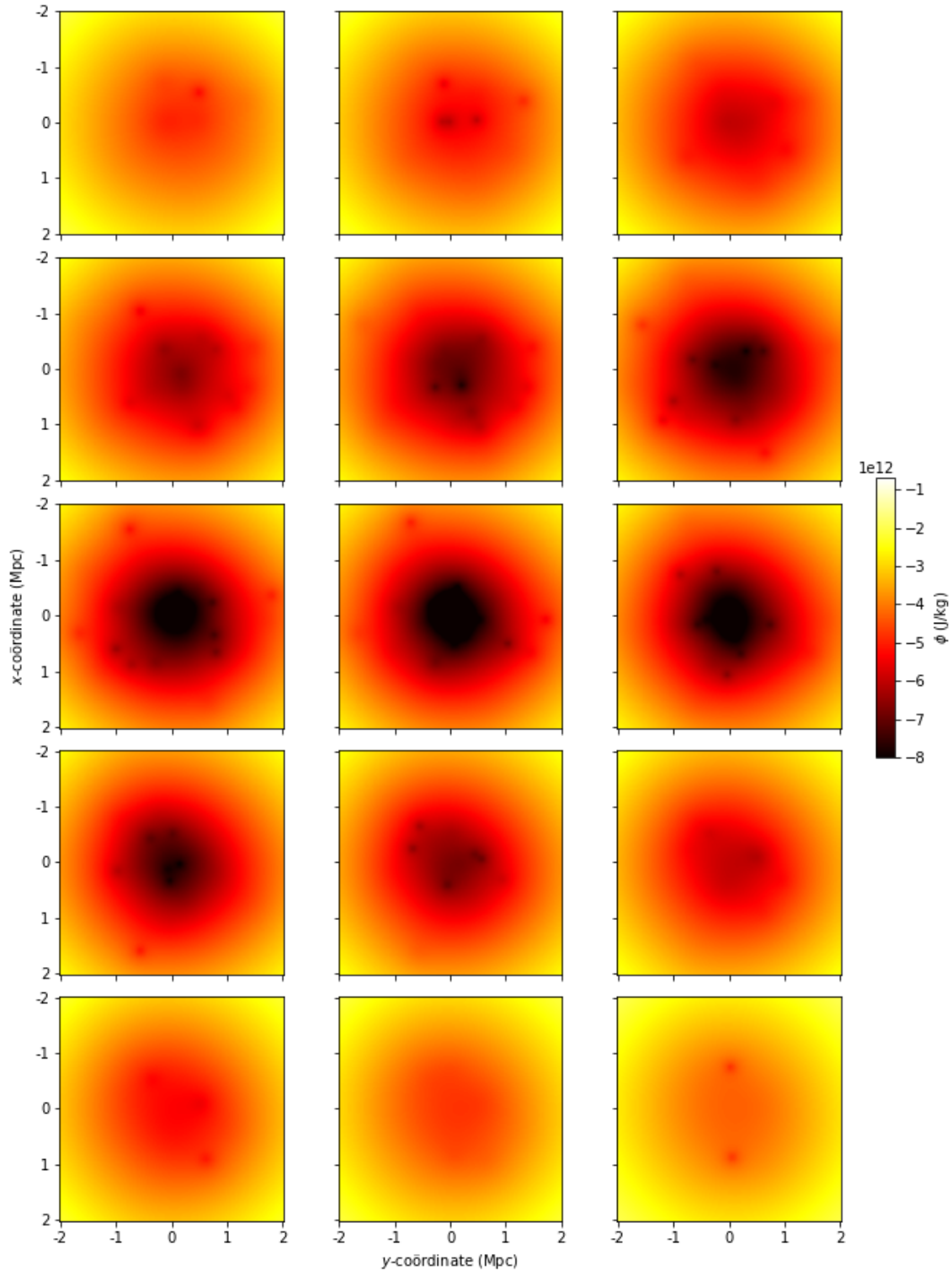


Figure 25: A plot of the full MOND potential, derived from the same initial mass distribution as Figure 16 with $N = 500$. The intersections are taken at $z = 0 + \frac{n}{4}$ Mpc, with $n = -7, -6, \dots, 6, 7$. The full MOND potential seems to follow the shape of the ND potential of Figure 16 at the center of the galaxy cluster, and of the deep MOND potential of Figure 17 at the outside.

$$N = 1500$$

Comparing Figures 24, 25 and 26 to those given in section 5.1 shows that the range of the potential is larger for full MOND, than for deep MOND and ND. This can be explained as follows. As already stated in Section 5.1 the ND potential is flat at the outsides, and very steep at the center of the galaxy clusters. The deep MOND potential is less steep at the center, and more steep at the outsides of the galaxy cluster. We see in Figures 24, 25 and 26 that the full MOND potential is steeper than the ND potential at the outsides of the galaxy cluster. In this region it seems to behave the same way as the deep MOND potential. We also see that the full MOND potential is steeper than the deep MOND potential at the center of the galaxy cluster, where it seems closer to the ND potential. So it makes sense that the full range of the full MOND potential is larger than those of the deep MOND and the ND potential.

That the full MOND potential follows the shape of the deep MOND potential at the outside of the cluster, and the ND potential at the center, suggests that the acceleration f is larger than a_0 in the center, and smaller than a_0 at the outside. We also suspect this because Figure 20 confirms this for deep MOND. We compute and discuss acceleration field f for full MOND in the next section.

6.2. Acceleration

In this section we will discuss the acceleration that is generated by the full MOND potential ϕ_{Mfull} of a certain mass distribution ρ . We found the acceleration by applying the Poisson equation to the full MOND potential given in Figure 24.

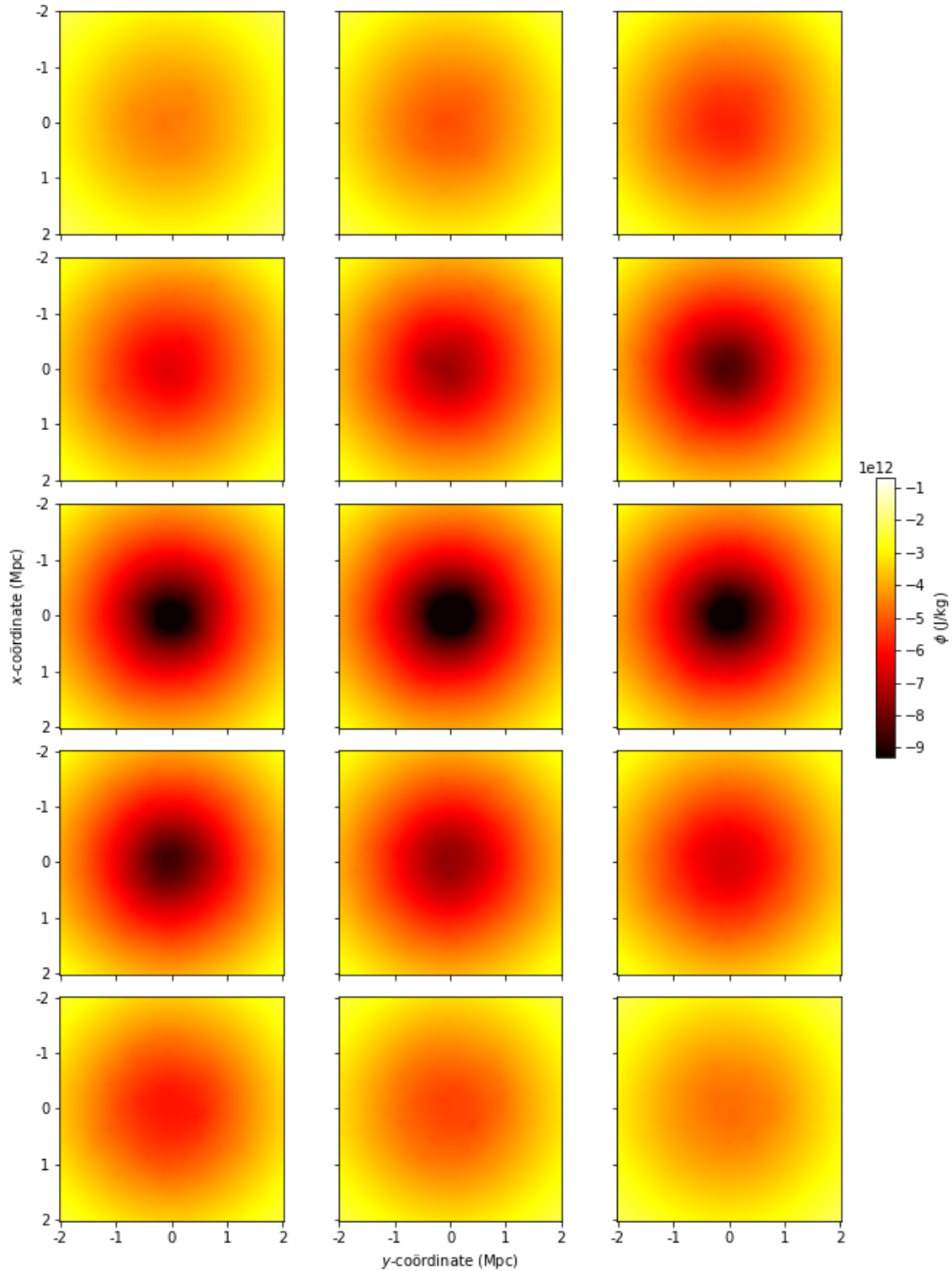


Figure 26: A plot of the full MOND potential, derived from the same initial mass distribution as Figure 18 with $N = 1500$. The intersections are taken at $z = 0 + \frac{n}{4}$ Mpc, with $n = -7, -6, \dots, 6, 7$. The full MOND potential seems to follow the shape of the ND potential of Figure 18 at the center of the galaxy cluster, and of the deep MOND potential of Figure 19 at the outside. The potential is almost spherically symmetric.

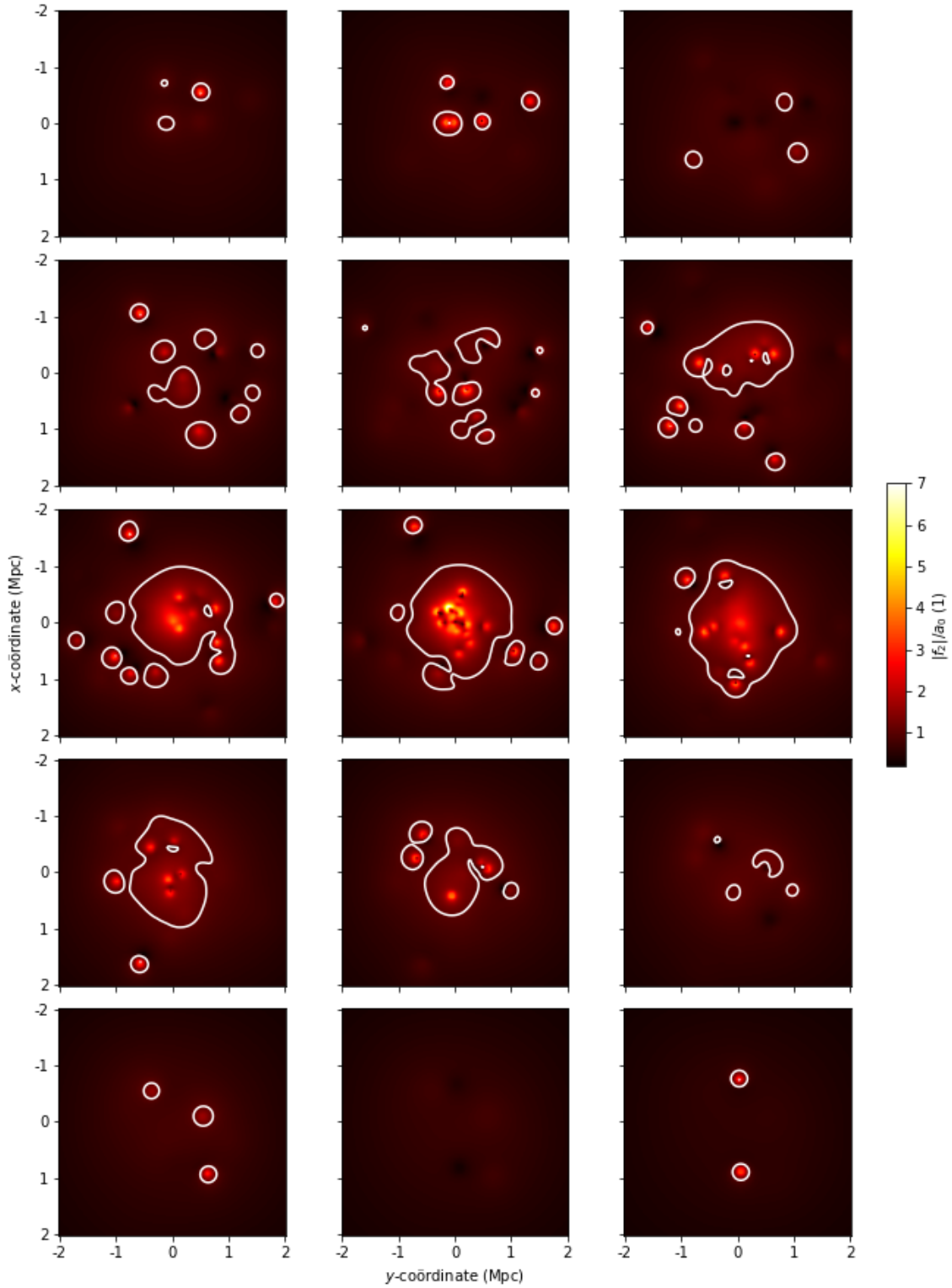


Figure 27: A plot of the size of the acceleration field f divided by a_0 , derived with full MOND from the same initial mass distribution as in Figure 14. The white curve corresponds to $|f|/a_0 = 1$. The intersections are taken at $z = 0 + \frac{n}{4}$ Mpc, with $n = -7, -6, \dots, 6, 7$. There are large regions where $f > a_0$, but there are also large regions where $f < a_0$.

In Figure 27 it is visible that the acceleration f in the galaxy cluster is both above and below a_0 in large regions. This was expected since this was also the case in Figure 20, and since the full MOND potential in Figure 14 showed deep MOND behaviour at the outside of the cluster, and ND behaviour at the inside.

We made a Figure similar to Figure 27 for $N = 1500$, to see whether for larger N the galaxy cluster still contained areas with f larger than a_0 and areas with f smaller than a_0 . This is expected for the same reasons as was for the galaxy cluster with $N = 100$. The acceleration field was found by applying the Poisson equation to the full MOND potential given in Figure 26.

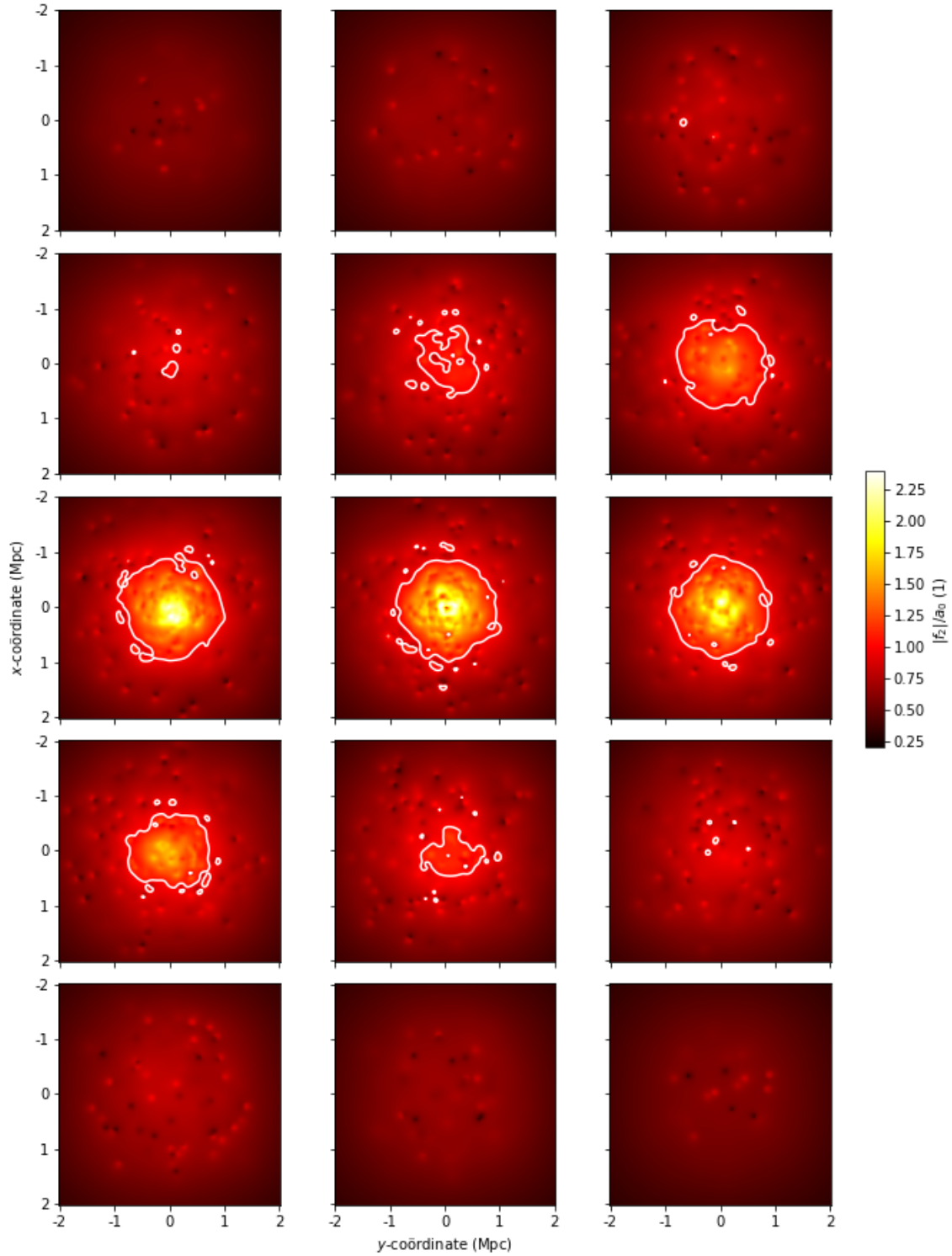


Figure 28: A plot of the size of the acceleration field f divided by a_0 , derived with full MOND from the same initial mass distribution as in Figure 18. The white curve corresponds to $|f|/a_0 = 1$. The intersections are taken at $z = 0 + \frac{n}{4}$ Mpc, with $n = -7, -6, \dots, 6, 7$. There are large regions where $f > a_0$, but there are also large regions where $f < a_0$.

Indeed the acceleration f is both smaller and larger than a_0 in large regions of the galaxy clus-

ter.

6.3. Apparent matter

In this section we will discuss the apparent matter needed to represent the results of MOND in the framework of DM. Figure 29 gives the apparent matter distribution derived with full MOND and based on the same mass distribution as used for Figure 14.

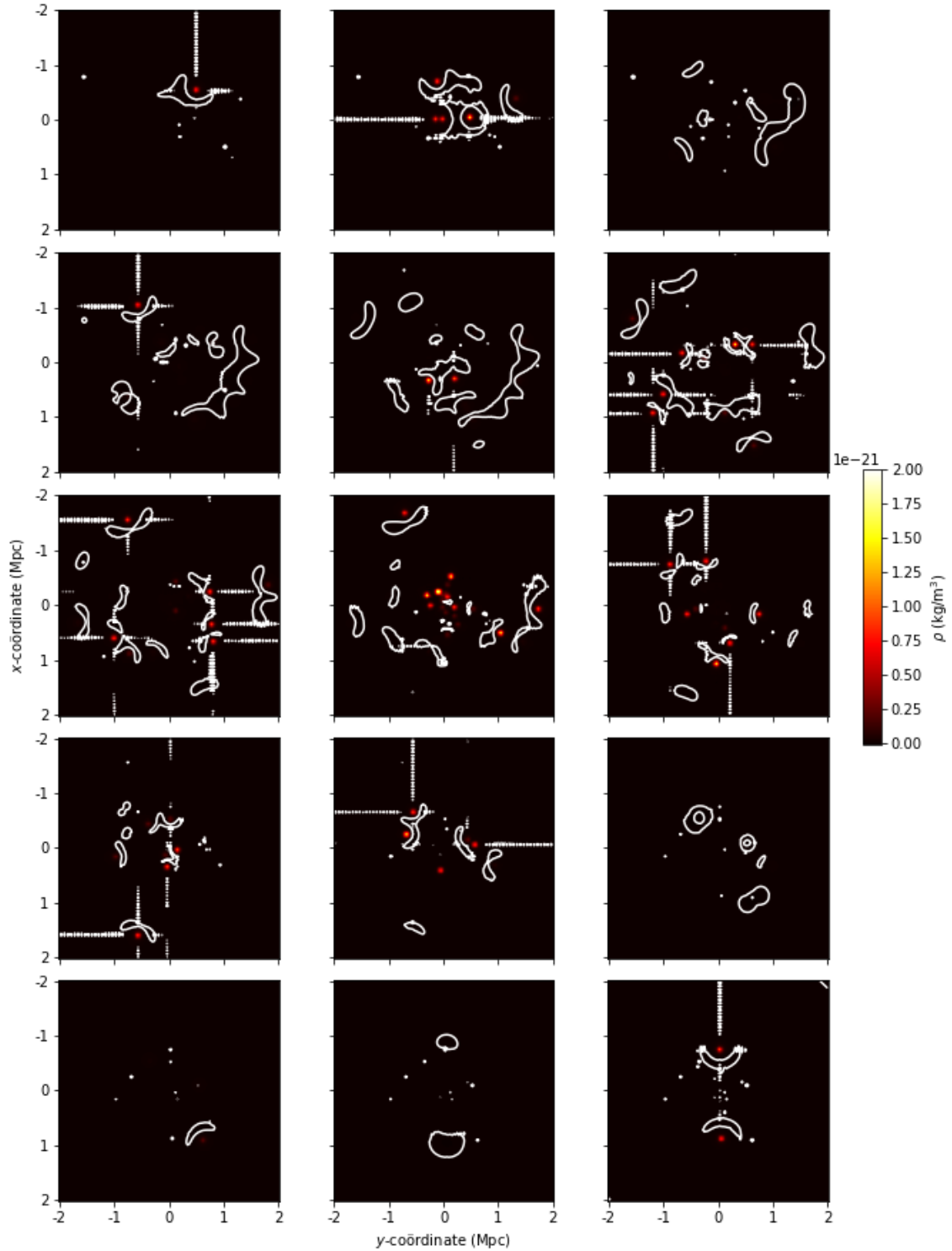


Figure 29: A plot of the apparent dark matter distribution derived with full MOND from the same initial mass distribution as in Figure 14. The white curve corresponds to $\rho = 0$. The intersections are taken at $z = 0 + \frac{n}{4}$ Mpc, with $n = -7, -6, \dots, 6, 7$. There are significant areas where $\rho_{AM} \leq 0$, and they all seem to be located inbetween galaxies. The dotted crosses are artefacts of the Fourier transform that is used to derive the distribution.

In Figure 29 we also see some areas in which $\rho \leq 0$. These negative apparent mass densities are no reason to question our methods, for the same reason as in Section 5 [2]. We will again compute the total negative apparent mass M_- in the next Section.

Similarly to the apparent mass distribution we derived with deep MOND, the regions where $\rho_{AM} \leq 0$ seem to occur inbetween masses. Again, this is in agreement with what Milgrom found [2]. If we compare Figure 29 to Figure 27, we can see that the areas where $\rho_{AM} \leq 0$ also mostly occur right outside the regions where $f \geq a_0$. However, similarly to the observations in Section 5.3, there are also regions where $\rho_{AM} \leq 0$ and $f \geq a_0$. Therefore it is still hard to determine a clear relation between f and ρ_{AM} , this is something that could be investigated in followup research. At the outside of the galaxy clusters, f becomes even smaller, and no negative apparent mass occurs. This is again in agreement with what Milgrom found.

There are also dotted crosses that have values around $\rho_{AM} = 0$, and again we suspect they are caused by the fourier transform.

6.4. Negative apparent matter

In this section we will discuss results similar to those discussed in Section 5.4, now derived with full MOND. For this we define and compute ρ_- and M_- in the same way as in Section 5.4. We will first vary the radius R_{sphere} of the galaxies of a galaxy cluster, next we will vary the number of galaxies N in the galaxy cluster. By the same reasoning as in Section 5.4, we expect that if R_{sphere} or N increases, and thus the initial mass distribution ρ becomes more spherically symmetric, then the negative apparent mass M_- decreases.

6.4.1. Changing the radius of galaxies

Results similar to those in section 5.4.1 are given, now derived with full MOND.

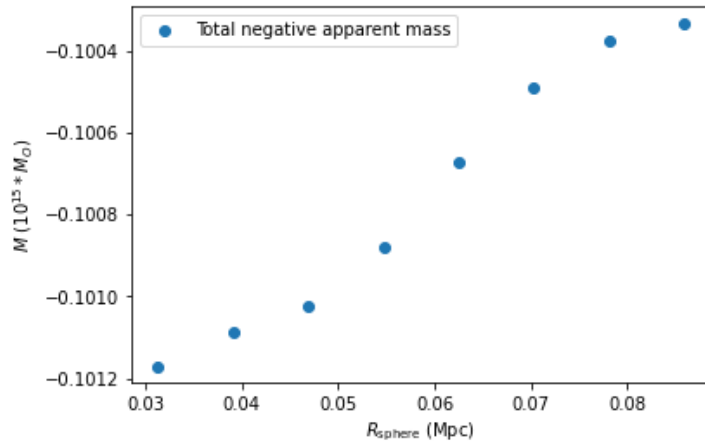


Figure 30: The negative apparent mass M_- , plotted against the radius R_{sphere} of the galaxies in a galaxy cluster with $N = 100$. The blue circles give the sum of the negative part of the apparent mass distribution ρ_- . M_- is derived with full MOND. There is a clear relation between R_{sphere} and M_- .

We can clearly see that when R_{sphere} is increased, the negative apparent mass becomes smaller.

6.4.2. Changing the number of galaxies

Results similar to those in Section 5.4.2 are given, now derived with full MOND.

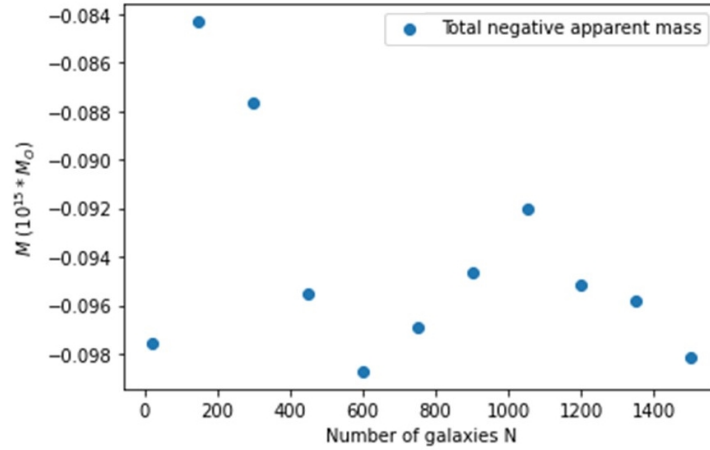


Figure 31: The negative apparent mass M_- , plotted against the number of galaxies N in the galaxy cluster with $R_{\text{sphere}} = 8/256$ Mpc. The blue circles give the sum of the negative part of the apparent mass distribution ρ_- . M_- is derived with full MOND. There is no clear relation between N and M_- .

Similarly to Figure 23, in Figure 31 no clear relation is visible between the number of galaxies N and the negative apparent mass M_- . This can be explained by the same reasoning as in Section 5.4.2.

6.4.3. Discussion of the negative apparent matter in full MOND

In this section we see similar results as in Section 5.4. So again, we have that when ρ becomes smoother, the negative apparent mass M_- decreases. Also the amount of negative apparent mass in a cluster with $N = 1500$ and $R_{\text{sphere}} = 8/256$ Mpc, is of the order $M_- \approx -0.09M$. Therefore we can conclude that also with full MOND, realistic mass configurations can be generated that give a significant amount of negative apparent mass.

7. Discussion

In this section we will discuss the results found in this thesis. For various initial mass distributions ρ we computed their deep MOND potential ϕ_{Mdeep} , and their full MOND potential ϕ_{Mfull} . With these potentials we derived the acceleration fields $\mathbf{f} = -\nabla\phi_{\text{M}}$, the apparent mass distributions ρ_{AM} and computed the total negative apparent mass M_- . All these aspects will be discussed.

In Sections 5.1 and 6.1 we found that the full MOND potential gives a larger range in potential than the deep MOND and ND potential. In Figure 27 we found that for full MOND the acceleration f is smaller than a_0 at the outside of the galaxy cluster, and larger than a_0 at the center of the galaxy cluster. Therefore we expect the full MOND potential to follow deep MOND at the outside of the cluster, and ND at the center. Indeed at the outside, the full MOND potential was steeper than the ND potential, and seemed to follow the deep MOND potential. Also, at the inside the full MOND potential was steeper than the deep MOND potential and seemed to follow the ND potential.

For $N = 100$ we computed the acceleration field \mathbf{f} of the deep MOND and the full MOND potential. In both cases there are large areas with $f = |\mathbf{f}| < a_0$ and large areas with $f > a_0$. This was also done for $N = 1500$ in the full MOND regime, and got the same result. From this we conclude that the deep MOND assumption, that in the entire galaxy cluster $f \ll a_0$, is wrong for clusters like the Virgo cluster.

Next, we computed the apparent mass distribution for both the deep MOND as the full MOND potential with $N = 100$. In both cases we can see clear regions where $\rho_{\text{AM}} \leq 0$, and in both cases these regions appear inbetween masses, and are mostly outside of regions where $f \geq a_0$. The shape and location of these regions are in agreement with what Milgrom found [2], but we have not found a clear relation between f and ρ_{AM} . Furthermore, we see white dotted crosses at which $\rho_{\text{AM}} \approx 0$, we suspect these are artefacts caused by the Fourier transform.

To further investigate the areas with a negative apparent mass distribution we computed the total negative apparent mass M_- . We did this for multiple mass distributions, varying the galaxies their radius R_{sphere} , and the number of galaxies N . Varying the radius of the galaxies gave us Figures 22, and 30. From these we conclude that for both deep and full MOND, when the initial mass density becomes smoother, the total negative apparent mass M_- becomes smaller. However, this was not clear from Figures 23 and 31. This can be explained by the fact that changing the radius has a much larger effect on the smoothness of the mass distribution ρ , than the number of galaxies N . Also, for each different N a new random galaxy cluster was generated, creating a random element in M_- and explaining why the Figures are chaotic. However, both for deep and full MOND, we see that for all values N and R_{sphere} , including values based on the Virgo cluster, the amount of negative apparent mass is of the order $M_- \approx -0.09M$. Thus there exist realistic mass distributions that generate a significant amount of negative apparent mass M_- according to MOND with our method.

The observation that realistic mass configurations exist that generate a significant amount of negative apparent mass, gives the opportunity to create falsification conditions. Suppose that we find a galaxy cluster with a visible matter distribution ρ and lensing observations that the MOND potential ϕ_{M} predicts correctly. Then MOND works correctly. Now if this potential ϕ_{M}

also predicts apparent negative mass M_- , then the DM model is falsified, since negative mass is impossible in any model.

Furthermore, we can also create falsification conditions for MOND with this observation. Namely if all potentials ϕ found with lensing observations give no negative apparent mass M_- , then the MOND potentials ϕ_M that correspond to negative apparent mass cannot be correct. In that case, the MOND model would be falsified.

Lastly, we see that most results of deep and full MOND are similar. There are quantitative differences, but we can derive the same conclusions from them. Although for example Figure 20 allowed us to conclude that deep MOND is based on wrong assumptions, these similarities show that the asymptotic behaviour of MOND (i.e. deep MOND) is still relevant to create a qualitative awareness about MOND.

8. Conclusion and recommendations

In this section we will summarize our conclusions and give some recommendations.

We found that the full MOND potential ϕ_{Mfull} follows the deep MOND potential ϕ_{Mdeep} at the outside of Virgo-like galaxy clusters, and it follows the ND potential ϕ_{ND} at the center of Virgo-like galaxy clusters. This suggests that the behaviour of galaxy clusters like Virgo cannot be approximated with deep MOND, and thus need an interpolation function μ in the MOND model to be accurate.

This conclusion can also be drawn from the Figures of the acceleration fields f in both deep MOND and full MOND. In all three Figures 20, 27 and 28 there are large regions where f is larger than a_0 , and large regions where f is smaller than a_0 . Again suggesting that the clusters behaviour cannot be described with ND or deep MOND, and only by full MOND.

Another result is that we can generate realistic mass distributions ρ that give an apparent mass distribution ρ_{AM} that is negative in some regions. The shape and location of these regions is in agreement with what Milgrom [2]. The total negative apparent mass M_- decreases when the initial mass distribution ρ becomes smoother. However, we found that galaxy clusters like the Virgo cluster do give a significant amount of negative apparent mass M_- with our method. Namely of the order $M_- \approx 0.09M$, with M the total mass of the actual mass distribution ρ .

Therefore we can set up falsification conditions for the DM model. Suppose that we can find a galaxy cluster with a visible matter distribution ρ where MOND predicts a potential ϕ_{M} that correctly predicts the lensing observations. Then the MOND model seems to work. Now if this potential ϕ_{M} also predicts negative apparent mass M_- , then the DM model would be falsified, because in DM and any other model, negative mass is impossible.

We can also set up falsification conditions for the MOND model. If all potentials ϕ found with lensing observations give no negative apparent mass M_- , then the potentials ϕ_{M} that MOND predicts to give negative matter cannot be correct. Thus, the MOND model is falsified.

Some recommendations for followup research are now given. Firstly the effect of different interpolation functions μ can be investigated. This could have effect on the full MOND potential ϕ_{Mfull} , the acceleration f , and the amount of negative apparent mass M_- .

Another recommendation is to investigate the effect of the initial mass distribution, and the probability function that is used to generate it. We chose to generate the initial mass distribution with the NFW profile. However the NFW profile gives a mass distribution for dark matter halos, and we generated a mass distribution of visible mass in a galaxy cluster. The isothermal sphere profile however, would also have been an incorrect choice of initial mass distribution, since it has been designed to satisfy the hydrostatic equilibrium, which is an equilibrium based on ND. In followup research, a distribution could be found in the same way as the isothermal sphere profile, satisfying the MOND equation (23).

In this thesis we saw that the regions where the apparent mass distribution $\rho_{\text{AM}} \leq 0$ were mostly located outside of regions where the acceleration $f \geq a_0$. This suggests that there is some relation between f and ρ_{AM} . In followup research this could be investigated more in depth.

In the apparent mass distribution there were also dotted crosses visible where $\rho_{AM} \approx 0$ that are artefacts of the Fourier transform. To lessen the size of these artefacts the step size in the Fourier transform could be decreased in future research.

Lastly, Figures 23 and 31 did not show a clear relation between the number of galaxies N and the negative apparent mass M_- . We do expect such a relation to exist, and expect our chaotic results to be caused by random noise in our measurements. The random noise might decrease if M_- is calculated for multiple galaxy clusters with a particular number of galaxies N , and an average is computed. M_- could also be computed for much larger N , since then the random noise of M_- might become relatively small in comparison to the relation between N and M_- .

References

- [1] M. Milgrom. Mond-a pedagogical review. *Acta Physica Polonica B*, 32, September 2001.
- [2] M. Milgrom. Can the hidden mass be negative? *The Astrophysical Journal*, 306, July 1986.
- [3] F. Zwicky. Republication of: The redshift of extragalactic nebulae. 2008.
- [4] F. Zwicky. On the masses of nebulae and of clusters of nebulae. *Astrophysical Journal*, 86, October 1937.
- [5] T. Childers. Vera rubin: The astronomer who brought dark matter to light. <https://www.space.com/vera-rubin.html>. Accessed: 2021-09-21.
- [6] K. Freese. Status of dark matter in the universe. *International Journal of Modern Physics D*, 26, May 2017.
- [7] ESA/Hubble NASA. https://apod.nasa.gov/apod/image/1112/lensshoe_hubble_3235.jpg, 2007.
- [8] M. Milgrom. Modified newtonian dynamics rotation curves of very low mass spiral galaxies. *Astrophysical Journal*, 658, March 2007.
- [9] J.D. Bekenstein. The modified newtonian dynamics-mond and its implications for new physics. *Contemporary physics*, 47, March 2007.
- [10] W.D. McComb. *Dynamics and Relativity*. Oxford University Press Inc., 1999.
- [11] L. Devroye. *Non-Uniform Random Variate Generation*. Springer-Verlag New York Inc., 1986.
- [12] D. Welsh G. Grimmett. *Probability An Introduction*. Oxford University Press, 1986.
- [13] S. Hamid Nawab A.V. Oppenheim, A.A. Willsky. *Signals Systems*. Prentice-Hall, 1997.
- [14] V.E. Karachentseva O.G. Kashibadze, I.D. Karachentsev. Structure and kinematics of the virgo cluster of galaxies. *Astronomy & Astrophysics*, 635, March 2020.
- [15] P. Natarajan J.M. Comerford. The observed concentration–mass relation for galaxy clusters. *Monthly Notices of the Royal Astronomical Society*, 379, July 2007.
- [16] University of Vermont K.E. Oughstun. Helmholtz’ theorem. [https://web.archive.org/web/20120813005804/http://www.cems.uvm.edu/~oughstun/LectureNotes141/Topic_03_\(Helmholtz' %20Theorem\).pdf](https://web.archive.org/web/20120813005804/http://www.cems.uvm.edu/~oughstun/LectureNotes141/Topic_03_(Helmholtz'%20Theorem).pdf). Accessed: 2022-01-27.

Appendix A

All code used in this thesis was based on the code by W. Hajer (to be published on the TU Delft repository). In this appendix the functions that were used in the code are given, and the code to find the ND potential ϕ_{ND} , the full MOND potential ϕ_{Mfull} , the acceleration f , the apparent mass distribution ρ_{AM} and the negative apparent mass M_- is given. ϕ_{Mdeep} can be derived in a similar way, using the iterative process described in Section 4.5.1. How the Figures were made is not included in this appendix.

Definition functions

In this part of the appendix all functions that were used in this thesis are given.

```
1 # Mass in a ball of radius r with spherically symmetric mass distribution
  rho
2 def M_rad(r, rho):
3     def Mfunc(r_):
4         return 4*np.pi*r_**2*rho(r_)[0]
5     return integ.quad(Mfunc, a=0, b=r)
6
7 # pdf for gaussian distribution
8 def pdf2(x, s):
9     return np.e**(-x**2/(2*s**2))/(2*np.pi*s**2)**0.5
10
11 # Add a gaussian mass distribution with radius Rsphere at location x to
  mass distribution rhox
12 def rho_gaus2(x, rhox):
13     dxyz=x-y-z-x
14     dsqrd = np.sum(dxyz**2, axis=1)
15     for i in np.where(dsqrd<=Rsphere**2):
16         rhox[i] = rhox[i] + Msphere*pdf2(dxyz[i, 0], Rsphere/5)*pdf2(dxyz[i
  , 1], Rsphere/5)*pdf2(dxyz[i, 2], Rsphere/5)
17     return rhox
18
19 # ND potential of an arbitrary mass distribution
20 def phi_rad(r, rho):
21     res = np.zeros_like(r)
22     def phifunc(R_):
23         return G*M_rad(R_, rho)[0]*R_**(-2)
24     if type(r) == np.float64:
25         for i, val in enumerate(np.array([r])):
26             res[i] = integ.quad(phifunc, a=1, b=val)[0]
27     else:
28         for i, val in enumerate(r):
29             res[i] = integ.quad(phifunc, a=1, b=val)[0]
30     return res
31
32 # ND potential of NFW-profile
33 def phi_NFW(x):
34     return phi_rad((x.T[0]**2+x.T[1]**2+x.T[2]**2)**0.5, rho_NFW)
35
36 # Create a random location according to mass distribution rho
37 def rand(rho):
38     u = np.random.uniform()
```

```

39 v = np.random.uniform()
40 w = np.random.uniform()
41 def Finv(ran, rho):
42     def F_min_u(r):
43         return M_rad(r, rho) [0]/M_rad(rho(5) [1], rho) [0] - ran
44     return fsolve(F_min_u, x0 = rho(5) [1]/2)
45 return np.array([Finv(u, rho) [0], 2*np.pi*v, np.arccos(2*w-1)])
46
47 # Generate N random coordinates of mass M/N with mass distribution rho
48 def randClus(N, rho, M):
49     zero_vec = np.array([0.0, 0.0, 0.0])
50     x = np.array([zero_vec for i in range(N)])
51     m=M/N
52     for i in range(N):
53         x[i] = rand(rho)
54     return np.array([x, m])
55
56 # Constant mass distribution
57 def rho_cst(r):
58     R = 2*mpc
59     c = M*3/(4*np.pi*R**3)
60     out = np.where(r<R, c, 0.0)
61     return (out, R)
62
63 # Mass distribution for NFW-profile
64 def rho_NFW(r):
65     c = 3.8
66     R_vir = 2*mpc
67     A_NFW = np.log(1+c)-c/(1+c)
68     M_vir = M
69     rho_halo = 3*M_vir/(4*np.pi*R_vir**3)
70     out = np.where(r<R_vir, rho_halo*R_vir/(3*A_NFW*r*(c**(-1)+r/R_vir)**2),
71 ,0.0)
72     return(out, R_vir)
73
74 # Reshaping numpy arrays in a certain way
75 def reshape_3d(A):
76     Ax = np.concatenate((A[:, int((nsteps-1)/2):nsteps, :, :], A[:, 0:int((
77 nsteps-1)/2), :, :]), axis=1)
78     Axy = np.concatenate((Ax[:, :, int((nsteps-1)/2):nsteps, :], Ax[:, :, 0:int((
79 nsteps-1)/2), :]), axis=2)
80     Axyz = np.concatenate((Axy[:, :, :, int((nsteps-1)/2):nsteps], Axy[:, :, :, 0:
81 int((nsteps-1)/2)]), axis=3)
82     return Axyz
83
84 def reshape_3d_inv(Axyz):
85     Axy = np.concatenate((Axyz[:, int(1+(nsteps-1)/2):nsteps, :, :], Axyz[:, 0:
86 int(1+(nsteps-1)/2), :, :]), axis=3)
87     Ax = np.concatenate((Axy[:, :, int(1+(nsteps-1)/2):nsteps, :], Axy[:, :, 0:
88 int(1+(nsteps-1)/2), :]), axis=2)
89     A = np.concatenate((Ax[:, :, :, int(1+(nsteps-1)/2):nsteps], Ax[:, :, :, 0:int
90 (1+(nsteps-1)/2)]), axis=1)
91     return A
92
93 def reshape_1d(A):

```

```

87     Ax = np.concatenate((A[int((nsteps-1)/2):nsteps, :, :], A[0:int((nsteps-1)
100 /2), :, :]), axis=0)
88     Axy = np.concatenate((Ax[:, int((nsteps-1)/2):nsteps, :], Ax[:, 0:int((
100 nsteps-1)/2), :]), axis=1)
89     Axyz = np.concatenate((Axy[:, :, int((nsteps-1)/2):nsteps], Axy[:, :, 0:int
100 ((nsteps-1)/2)]), axis=2)
90     return Axyz
91
92 def reshape_1d_inv(Axyz):
93     Axy = np.concatenate((Axyz[int(1+(nsteps-1)/2):nsteps, :, :], Axyz[0:int
100 (1+(nsteps-1)/2), :, :]), axis=2)
94     Ax = np.concatenate((Axy[:, int(1+(nsteps-1)/2):nsteps, :], Axy[:, 0:int
100 (1+(nsteps-1)/2), :]), axis=1)
95     A = np.concatenate((Ax[:, :, int(1+(nsteps-1)/2):nsteps], Ax[:, :, 0:int(1+(
100 nsteps-1)/2)]), axis=0)
96     return A
97
98 #Iterative proces for deep MOND
99 def f_iterate(fnx, fny, fnz):
100     fnx_tilde, fny_tilde, fnz_tilde = np.fft.fftn(fnx), np.fft.fftn(fny), np.
100     fft.fftn(fnz)
101     k_dot_fn_tilde = Kx*fnx_tilde + Ky*fny_tilde + Kz*fnz_tilde
102     fnlx_tilde = Kx*k_dot_fn_tilde*kxyz_inv**2
103     fnly_tilde = Ky*k_dot_fn_tilde*kxyz_inv**2
104     fnlz_tilde = Kz*k_dot_fn_tilde*kxyz_inv**2
105     fnlx, fnly, fnlz = np.fft.ifftn(fnlx_tilde), np.fft.ifftn(fnly_tilde), np.
105     fft.ifftn(fnlz_tilde)
106     return fnlx, fnly, fnlz
107
108 #Iterative proces for deep MOND
109 def B_iterate(fnlx, fnly, fnlz):
110     fnl = np.sum([fnlx**2, fnly**2, fnlz**2], axis=0)**0.5
111     Bnlx = fnl*fnlx-gx*a0
112     Bnly = fnl*fnly-gy*a0
113     Bnlz = fnl*fnlz-gz*a0
114     Bnlx_tilde, Bnly_tilde, Bnlz_tilde = np.fft.fftn(Bnlx), np.fft.fftn(Bnly),
100     np.fft.fftn(Bnlz)
115     k_dot_Bn1_tilde = Kx*Bnlx_tilde + Ky*Bnly_tilde + Kz*Bnlz_tilde
116     Bn2x_tilde = Bnlx_tilde - Kx*k_dot_Bn1_tilde*kxyz_inv**2
117     Bn2y_tilde = Bnly_tilde - Ky*k_dot_Bn1_tilde*kxyz_inv**2
118     Bn2z_tilde = Bnlz_tilde - Kz*k_dot_Bn1_tilde*kxyz_inv**2
119     Bn2x, Bn2y, Bn2z = np.fft.ifftn(Bn2x_tilde), np.fft.ifftn(Bn2y_tilde), np.
100     fft.ifftn(Bn2z_tilde)
120     Fn2x, Fn2y, Fn2z = gx*a0+Bn2x, gy*a0+Bn2y, gz*a0+Bn2z
121     Fn2 = np.sum([Fn2x**2, Fn2y**2, Fn2z**2], axis=0)**0.5
122     fn2x, fn2y, fn2z = Fn2x*Fn2**-0.5, Fn2y*Fn2**-0.5, Fn2z*Fn2**-0.5
123     return fn2x, fn2y, fn2z
124
125 #Iterative proces for full MOND
126 def f_it_int(fnx, fny, fnz):
127     fnx_tilde, fny_tilde, fnz_tilde = np.fft.fftn(fnx), np.fft.fftn(fny), np.
100     fft.fftn(fnz)
128     k_dot_fn_tilde = Kx*fnx_tilde + Ky*fny_tilde + Kz*fnz_tilde
129     fnlx_tilde = Kx*k_dot_fn_tilde*kxyz_inv**2
130     fnly_tilde = Ky*k_dot_fn_tilde*kxyz_inv**2

```

```

131     fnlz_tilde = Kz*k_dot_fn_tilde*kxyz_inv**2
132     fnlx,fnly,fnlz = np.fft.ifftn(fnlx_tilde),np.fft.ifftn(fnly_tilde),np.
133     fft.ifftn(fnlz_tilde)
134     return fnlx,fnly,fnlz
135 #Iterative proces for full MOND
136 def B_it_int(fnlx,fnly,fnlz):
137     fnl = np.sum([fnlx**2,fnly**2,fnlz**2],axis=0)**0.5
138     Bnlx = fnlx*fnl/(a0**2+fnl**2)**0.5-gx
139     Bnly = fnly*fnl/(a0**2+fnl**2)**0.5-gy
140     Bnlz = fnlz*fnl/(a0**2+fnl**2)**0.5-gz
141     Bnlx_tilde,Bnly_tilde,Bnlz_tilde = np.fft.fftn(Bnlx),np.fft.fftn(Bnly),
142     np.fft.fftn(Bnlz)
143     k_dot_Bnl_tilde = Kx*Bnlx_tilde + Ky*Bnly_tilde + Kz*Bnlz_tilde
144     Bn2x_tilde = Bnlx_tilde - Kx*k_dot_Bnl_tilde*kxyz_inv**2
145     Bn2y_tilde = Bnly_tilde - Ky*k_dot_Bnl_tilde*kxyz_inv**2
146     Bn2z_tilde = Bnlz_tilde - Kz*k_dot_Bnl_tilde*kxyz_inv**2
147     Bn2x,Bn2y,Bn2z = np.fft.ifftn(Bn2x_tilde),np.fft.ifftn(Bn2y_tilde),np.
148     fft.ifftn(Bn2z_tilde)
149     Fn2x,Fn2y,Fn2z = gx+Bn2x,gy+Bn2y,gz+Bn2z
150     Fn2 = np.sum([Fn2x**2,Fn2y**2,Fn2z**2],axis=0)**0.5
151     fn2x = Fn2x*(0.5+(a0**2+Fn2**2/4)**0.5/Fn2)**0.5
152     fn2y = Fn2y*(0.5+(a0**2+Fn2**2/4)**0.5/Fn2)**0.5
153     fn2z = Fn2z*(0.5+(a0**2+Fn2**2/4)**0.5/Fn2)**0.5
154     return fn2x,fn2y,fn2z

```

Code for finding the ND and full MOND potential, the acceleration field, the apparent mass distribution and the total negative apparent mass

In this part of the appendix it is described how the ND potential ϕ_{ND} , the full MOND potential ϕ_{Mfull} , the acceleration f , the apparent mass distribution ρ_{AM} and the negative apparent mass M_- are derived. ϕ_{Mdeep} can be derived in a similar way, using the iterative proces described in Section 4.5.1.

```

1 #Importing
2 import scipy.integrate as integ
3 import numpy as np
4 from scipy.optimize import fsolve
5 import scipy.stats as stat
6 import matplotlib.pyplot as plt
7
8 #Constants
9 ly = 9.4605284 *10**15 #m           Light year
10 mpc = 3.26 *10**6 *ly #m          Megaparsec
11 M_O = 1.9891*10**30 #kg           Solar mass
12 G = 6.674 * 10**(-11) #m^3/kg/s^2 Gravitational constant
13 H0 = 72000/mpc # 1/s             Hubble constant
14 c = 2.998 * 10**(8) # m/s        Speed of light
15 a0 = c*H0/(2*np.pi) # m/s^2     Acceleration constant MOND
16 N = 1500                          # Number of galaxies
17 M = 10**15*M_O                    # Total mass
18 R = 2*mpc                         # Radius galaxy cluster
19 nsteps = 257
20 nstepsc = 257j

```

```

21 dv = (2*2*R/(nsteps-1))**3
22 dx = 2*2*R/(nsteps-1)
23 Msphere = M/N
24 Rsphere = 5*dx # straal sphere
25 d = M*3/(N*4*np.pi*Rsphere**3) # dichtheid sphere
26
27 #Define xyz space
28 xyz = np.mgrid[-2*R:2*R:nstepsc,-2*R:2*R:nstepsc,-2*R:2*R:nstepsc].reshape
    (3,-1).T #mesh of 513x513x513 points
29 rxyz = np.sum(xyz**2,axis=0)**0.5
30
31 #Define K space
32 Kvector = np.mgrid[-np.pi/dx:np.pi/dx:nstepsc, -np.pi/dx:np.pi/dx:nstepsc,-
    np.pi/dx:np.pi/dx:nstepsc]
33 Kxyz = reshape_3d(Kvector)
34 Kx = Kxyz[0]
35 Ky = Kxyz[1]
36 Kz = Kxyz[2]
37 kxyz = np.sum(Kxyz**2,axis=0)**0.5 #find the lenght of all k vectors
38 kxyz_inv = 1/kxyz
39 kxyz_inv[0,0,0]=0
40
41 # Generate random mass distribution
42 clus = randClus(N,rho_NFW,M)[0]
43 zero_vec = np.array([0.0,0.0,0.0])
44 clusxyz = np.array([zero_vec for i in range(N)])
45 for i in range(N):
46     clusxyz[i] = np.array([clus[i][0]*np.cos(clus[i][1])*np.sin(clus[i][2])
    ,clus[i][0]*np.sin(clus[i][1])*np.sin(clus[i][2]),clus[i][0]*np.cos(clus
    [i][2])])
47 clus_ijk = np.round(clusxyz*256/(8*mpc)).astype('int')
48 clus_int = clus_ijk*8*mpc/256
49 rho = np.zeros(nsteps**3)
50 for i in range(N):
51     rho = rho_gaus2(clus_int[i],rho)
52 rho = rho.reshape(nsteps,nsteps,nsteps)
53
54 # Find ND potential
55
56 rhotilde = np.fft.fftn(rho)#,np.array([nsteps,nsteps,nsteps])).astype('
    float64')
57 phi_N_tilde = -4*np.pi*G*rhotilde*kxyz_inv**2
58 phi_N = np.fft.ifftn(phi_N_tilde).astype('float64')
59
60 # Calculate vector field g
61 gx_tilde = 1j*np.multiply(Kx,phi_N_tilde)
62 gy_tilde = 1j*np.multiply(Ky,phi_N_tilde)
63 gz_tilde = 1j*np.multiply(Kz,phi_N_tilde)
64 gx = np.fft.ifftn(gx_tilde)
65 gy = np.fft.ifftn(gy_tilde)
66 gz = np.fft.ifftn(gz_tilde)
67 #Length of g
68 g = np.sum([gx**2,gy**2,gz**2],axis=0)**0.5
69 g_inv = 1/g
70 for i in range(0,nsteps):

```

```

71     for k in range(0,nsteps):
72         for l in range(0,nsteps):
73             if g[i,k,l]==0:
74                 g_inv[i,k,l]=0 #Wouter had heir 1 ipv 0, maakt niet uit
75                 want je vermenigvuldigt ook met gx,gy,gz, en die zijn 0 op deze locaties
76 # Calculate f0
77 f0xI = gx*(0.5+(a0**2+g**2/4)**0.5*g_inv)**0.5
78 f0yI = gy*(0.5+(a0**2+g**2/4)**0.5*g_inv)**0.5
79 f0zI = gz*(0.5+(a0**2+g**2/4)**0.5*g_inv)**0.5
80 # Iterate n times
81 n = 2
82 for i in range(n):
83     flxI,fllyI,flzI = f_it_int(f0xI,f0yI,f0zI)
84     f2xI,f2yI,f2zI = B_it_int(flxI,fllyI,flzI)
85     f0xI,f0yI,f0zI = f2xI,f2yI,f2zI
86 ffxI,fflyI,ffzI = f0xI,f0yI,f0zI
87
88 # Find MOND potential
89 ffx_tildeI,ffly_tildeI,ffz_tildeI = np.fft.fftn(ffxI),np.fft.fftn(fflyI),np.
90     fft.fftn(ffzI)
91 phi_M_tildeI = -lj*(Kx*ffx_tildeI + Ky*ffly_tildeI + Kz*ffz_tildeI)*kxyz_inv
92     **2
93 phi_MI = np.fft.ifftn(phi_M_tildeI).astype('float64')
94
95 # Find relative size of acceleration field fn
96 f_n_over_a0I = (np.sum([ffxI**2,fflyI**2,ffzI**2],axis=0)**0.5/a0).astype('
97     float64')
98
99 # Find apparent mass distribution
100 rho_dark_tildeI = - kxyz**2 * phi_M_tildeI / (4*np.pi*G)
101 rho_darkI = np.fft.ifftn(rho_dark_tildeI).astype('float64')
102
103 # Find negative apparent mass
104 dark = rho_dark[np.where(rxyz<=2*mpc)]
105 M_neg = np.sum(dark[np.where(dark<0)])*dv

```